

RICE UNIVERSITY

**Symmetry Breaking in Plasmonic Nanostructures**

by

**Mark W. Knight**

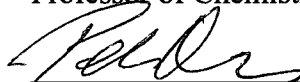
A THESIS SUBMITTED  
IN PARTIAL FULFILLMENT OF THE  
REQUIREMENTS FOR THE DEGREE

**Master of Science**

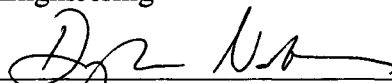
APPROVED, THESIS COMMITTEE:



Naomi J. Halas, Chair  
Stanley C. Moore Professor of  
Electrical and Computer Engineering  
Professor of Chemistry



Peter J. Nordlander  
Professor of Physics and Astronomy  
Professor of Electrical and Computer  
Engineering



Douglas Natelson  
Associate Professor of Physics and  
Astronomy  
Associate Professor of Electrical and  
Computer Engineering

HOUSTON, TEXAS

OCTOBER 2008

UMI Number: 1466790

### INFORMATION TO USERS

The quality of this reproduction is dependent upon the quality of the copy submitted. Broken or indistinct print, colored or poor quality illustrations and photographs, print bleed-through, substandard margins, and improper alignment can adversely affect reproduction.

In the unlikely event that the author did not send a complete manuscript and there are missing pages, these will be noted. Also, if unauthorized copyright material had to be removed, a note will indicate the deletion.

UMI<sup>®</sup>

---

UMI Microform 1466790

Copyright 2009 by ProQuest LLC

All rights reserved. This microform edition is protected against unauthorized copying under Title 17, United States Code.

---

ProQuest LLC  
789 East Eisenhower Parkway  
P.O. Box 1346  
Ann Arbor, MI 48106-1346

# **Abstract**

## **Symmetry Breaking in Plasmonic Nanostructures**

by

Mark W. Knight

The plasmonic properties of metallodielectric nanostructures exhibit a highly sensitive dependence on geometry due to the interaction between primitive plasmon modes associated with the surfaces of the nanoparticle. Breaking symmetry increases the interactions between plasmon modes giving rise to modified, and altogether new, plasmonic features. This thesis examines the effects of breaking symmetry on three variants of a core-shell nanoparticle and a nanoparticle-nanowire plasmonic waveguide. For asymmetric core-shell nanoparticles, the far field absorption and scattering properties and the near field enhancements depend strongly on the degree of asymmetry. For nanowires, adding a vicinal nanoparticle breaks cylindrical symmetry and permits polarization-dependent coupling of visible light to propagating wire plasmons. These results offer a potential strategy for tailoring the near and far field properties of plasmonic nanoparticle systems for specific applications including high performance surface-enhanced spectroscopy, bioimaging, nanoparticle-based therapeutics, and subwavelength nanoantennae for coupling into extreme subwavelength waveguides.

## Acknowledgements

I would first like to thank my advisor, Naomi Halas, and my co-advisor, Peter Nordlander, who together provided the resources, encouragement, excitement, and physical insight that made this thesis possible.

I am grateful to all those who guided me along my academic path, especially Jody House, who welcomed me into her lab at the Oregon Graduate Institute as an inexperienced high school student and has continued to provide friendship, insight, and guidance during my journey through college and my time at Rice University.

I would like to thank all the Halas group members who infused my research with fresh ideas and thoughtful criticism. In particular, I must thank Nate Grady who went above, and significantly beyond, the call of duty in sharing his experience with optics. I am grateful to Britt Lassiter, Britain Willingham, Nikolay Mirin, and Feng Hao for many discussions on the underlying physics of broken symmetry nanoparticles, Rizia Bardhan for her time on the SEM, and Felicia Tam for her assistance with chemical synthesis. I must also acknowledge Surbhi Lal, who has always been willing to accompany me to the Coffeehouse and spend another \$0.95 before looking over my writing.

I greatly appreciate the open door to Carolyn Aresu and Martha Alexander's office, where I regained my perspective on days when experiments failed and code crashed, and the stress-relief efforts of Joe Cole who provided me with a chainsaw and a tree.

Finally, I would like to thank my parents, Dick and Adela Knight, for starting me on my road to Rice with a violin and a microscope, and my brother Brian who always let me serve as 'test pilot' for our innumerable go-carts and zip lines.

# Table of Contents

<b>Abstract.....</b>	<b>ii</b>
<b>Acknowledgements .....</b>	<b>iii</b>
<b>Table of Contents .....</b>	<b>iv</b>
<b>List of Figures.....</b>	<b>v</b>
<b>Chapter 1: Introduction .....</b>	<b>1</b>
<b>Chapter 2: Nanoshells to Nanoeggs to Nanocups.....</b>	<b>3</b>
2.1 Introduction.....	3
2.2 Calculating nanoparticle spectra .....	4
2.3 Far field spectra of nanoparticles.....	7
2.4 Nanoegg near field properties.....	12
2.5 Tuning relative absorption and scattering efficiencies .....	15
2.6 Concluding remarks.....	16
<b>Chapter 3: Nanoparticle-mediated Coupling of Light and Nanowire Plasmons.....</b>	<b>18</b>
3.1 Introduction.....	18
3.2 Nanoparticle fabrication and optical characterization .....	19
3.3 Demonstration of polarization dependent coupling.....	21
3.4 Theoretical model .....	26
3.5 Concluding remarks.....	28
<b>Chapter 4: Summary .....</b>	<b>30</b>
<b>References.....</b>	<b>31</b>
<b>Appendix A: Defining Custom Dielectrics.....</b>	<b>36</b>
<b>Appendix B: Calculating the Near- and Far-field Properties of a Nanoshell .....</b>	<b>38</b>
<b>Appendix C: Space and Meshing Effects.....</b>	<b>51</b>

## List of Figures

<b>Figure 2.1.</b> Transformation of a nanoshell into a nanoegg or nanocup by core offset .....	3
<b>Figure 2.2.</b> Far field extinction properties of nanoshells, nanoeggs, and nanocups .....	11
<b>Figure 2.3.</b> Local field enhancements of nanoshells, nanoeggs, and nanocups .....	12
<b>Figure 2.4.</b> Local field enhancements of a nanoegg depending on mode order .....	14
<b>Figure 2.5.</b> Comparison of far-field absorption and scattering efficiencies.....	15
<b>Figure 3.1.</b> Optical layout used for nanowire excitation and characterization .....	20
<b>Figure 3.2.</b> Optical images showing coupling between photons and wire plasmons.....	22
<b>Figure 3.3.</b> Polarization-dependence of coupling efficiency .....	24
<b>Figure 3.4.</b> Geometry dependence of polarization angle for maximum emission .....	26
<b>Figure 3.5.</b> Finite element analysis of nanowire-nanoparticle geometry .....	28
<b>Figure B.1.</b> Creating a new 3D electrodynamics simulation in COMSOL.....	38
<b>Figure B.2.</b> Creating a spherical core.....	39
<b>Figure B.3.</b> Setting the outside of the PML as a scattering boundary.....	40
<b>Figure B.4.</b> Defining a far-field transform variable .....	41
<b>Figure B.5.</b> Setting the outer subspace as a PML .....	41
<b>Figure B.6.</b> Defining the shell subspace using the dielectric function.....	42
<b>Figure B.7.</b> Calculating the far-field absorption cross section of the nanoshell .....	43
<b>Figure B.8.</b> Calculating the far-field scattering cross section of the nanoshell .....	43
<b>Figure B.9.</b> Setting custom mesh visualization parameters .....	44
<b>Figure B.10.</b> Defining the incident plane wave in terms of free space wavelength.....	45
<b>Figure B.11.</b> Configuring the PARDISO linear system solver .....	46

<b>Figure B.12.</b> Plotting the absorption and scattering spectra .....	46
<b>Figure B.13.</b> Plotting a near field slice.....	47
<b>Figure C.1.</b> Schematic of the simulation space.....	51
<b>Figure C.2.</b> Extinction spectra for different simulation spaces.....	52
<b>Figure C.3.</b> Testing convergence at the dipole peak.....	53
<b>Figure C.4.</b> Dependence of the near-field enhancement on mesh size .....	54

# Chapter 1: Introduction

A rapidly expanding army of plasmonic nanostructures has taken the world of photonics by storm, offering solutions to decades-old problems and opening up new venues of exploration. These developments rely on plasmonic resonances, which are the collective oscillation of an electron gas, engineered to deliver near- and far-field optical properties specifically tailored for a given application [1].

Nanoshells, one example of a highly tunable nanoparticle, are formed of a thin coinage metal shell surrounding a dielectric core. By changing their relative inner and outer radii, and their absolute size, these particles can be optimized to deliver an intense near-field response, act as wavelength-specific absorbers, or scatter strongly at any desired wavelength from the visible to the mid-infrared. Nanoshells are already enabling cancer research to expand from a focus in pharmaceuticals and radiotherapy to include engineered nanoparticle therapies [2, 3], and revolutionizing spectroscopic measurements by providing field enhancements previously unavailable outside of specialized laser facilities [4-6]. Eventually, some variant of this metallodielectric nanoparticle may form the basis of an inexpensive optical metamaterial [7].

Nanoshells, due to their confined spatial extent, only support localized plasmon modes. Extended metallic structures, however, can support propagating plasmon modes. Exciting these modes optically in a controlled manner has become a topic of intense interest due to the technological promise of such waveguides. In particular, on-chip plasmonic waveguides compatible with complementary metal-oxide-semiconductor (CMOS) technology have theoretical data transmission rates more than 1000x greater



than state-of-the-art copper interconnects. If plasmonic wiring could be integrated on-chip, and fabricated at dimensions significantly smaller than the optical diffraction limit, processor performance could increase significantly [8, 9]. While significant progress on waveguiding has been demonstrated in nanoscale metallic dot arrays, [10, 11] metal-insulator-metal (MIM) structures, [12-14] and metallic nanowires [15-18], fundamental breakthroughs are still required before on-chip plasmonics can easily interface with the outside world.

This thesis will examine the fundamental effects of breaking the spherical symmetry of a nanoshell and the cylindrical symmetry of a plasmonic waveguide, and discuss how to further optimize these structures for potential real-world applications. The finite element method (FEM) will be used for electrodynamic modeling in both cases, with the results interpreted within the framework of plasmon hybridization theory. The model of light coupling into a nanowire waveguide through an adjacent nanoparticle will be corroborated with experimental observations of coupling between wire plasmons and photons and the measured effects of polarization on particle-based plasmon excitation efficiency [18, 19]. These two geometries demonstrate that controlled symmetry breaking can be an essential element in designing radically improved plasmonic components with tailored optical resonances [19, 20].

## Chapter 2: Nanoshells to Nanoeggs to Nanocups

### Optical Properties of Reduced Symmetry Core-Shell Nanoparticles Beyond the Quasistatic Limit

#### 2.1 Introduction

The near and far field optical properties of nanoshells, nanoeggs, and nanocups have been well studied individually [21-27]. This chapter will focus on the transitional behavior between these three classes of nanoparticle (Figure 2.1). Moving a spherical core away from the center of a spherical gold shell, and ultimately allowing it to emerge from the outer shell, effectively converts a nanoshell to a nanoegg, and then a nanocup, solely as a function of core offset. Examining the physical basis for calculated shifts in the plasmonic response may allow for the design of optimized, application specific nanoparticles. Reliably creating such particles to meet future industry demands may inspire the development of improved synthesis techniques.

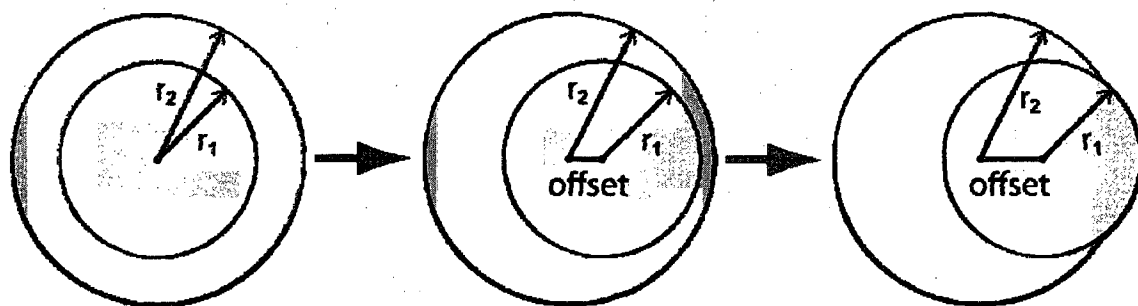


**Figure 2.1.** A symmetric silica-gold nanoshell can be transformed into an asymmetric nanoegg or nanocup by introducing a core offset.

The optical response of nanoshells can be calculated using Mie theory [28]; nanoeggs and nanocups require alternate methods of solution. In the quasistatic limit, where the size of the nanoparticle is substantially smaller than the vacuum wavelength of light, nanoeggs have been modeled analytically using plasmon hybridization theory [29, 30]. Determining the plasmonic properties of larger particles with a significant degree of asymmetry, such as nanoeggs and nanocups, require numerical methods of solution to include the effects of phase retardation.

In this chapter I have used the finite element method (FEM) to examine the transition from silica-gold nanoshells to nanoeggs and nanocups. Both the near and far field effects of core offset and total particle size are considered, with an emphasis on spectral evolution and focused field enhancements. I conclude that, for a given pair of inner and outer shell radii, phase retardation and core offsets can be used together to design nanoparticles with a desired scattering to absorption ratio at the dipolar resonance.

## **2.2 Calculating nanoparticle spectra**

The near- and far-field optical properties of nanoshells, nanoeggs, and nanocups were evaluated numerically in the frequency domain using the scattered field formulation. Problem definition, solution, and analysis were all conducted using Matlab (R2007a) in conjunction with the scripting functions of a commercially available FEM package (COMSOL Multiphysics 3.4 with the RF module).

The 3D simulation space was comprised of four spherical volumes: a core, a shell, an embedding medium, and a perfectly matched layer (PML). The nanoparticle core was silica ( $\epsilon_1 = 2.04$ ) embedded in a gold shell modeled using the empirically determined

bulk dielectric constants by Johnson and Christy with linear interpolation (Appendix A) [31]. The embedding medium was air. A plane wave, used for excitation, was inserted on the inside of the PML surrounding the embedding medium [32]. A detailed description of nanoshell simulations in COMSOL is provided in Appendix B.

The dimensions of the embedding volume and the PML layer were chosen such that increasing the size of the nanoparticle further would not affect the simulation results. For symmetric nanoshells, the absorption and extinction spectra calculated using COMSOL matched Mie theory in both extinction amplitude and peak wavelength (Figure 2.2(a), red dots).

Discretization of the simulation space was conducted using the built-in free meshing algorithm in COMSOL, which partitioned the simulation space into a collection of tetrahedral finite elements. Large field enhancements, resulting from plasmon resonances, required the application of mesh constraints to ensure convergence of the simulation in the visible and near infrared (NIR) ( $\lambda = 400 - 1500$  nm). The nanoshell and nanoegg surfaces were restricted to a maximum triangle mesh side length of 10 nm with an element growth rate of 1.40, specifying that elements adjoining the nanoparticle surface could be no more than 1.4 times the size of surface elements. Nanocups, where the abrupt core-shell intersection results in high field gradients, required a maximum edge mesh length of 1 nm and an element growth rate of 1.3 for convergence. Typical nanoparticle meshes using the constraints listed here resulted in  $1 \times 10^5 - 5 \times 10^5$  degrees of freedom (the number of parameters required to describe the scattered electric field in a simulation space). Additional details on choosing simulation spaces and mesh element dimensions

such that the FEM model will converge to the analytical solution for nanoshells are provided in Appendix C.

The core offset parameter  $D$  is defined as the dimensionless quantity  $D = \text{offset} / (r_2 - r_1)$ , where  $r_1$  and  $r_2$  are the radii of the nanoparticle core and shell, respectively. The  $D$  parameter defines particles in this chapter as nanoshells when  $D = 0$ , nanoeegs when  $0 < D < 1$ , and nanocups when  $D > 1$ . Due to unphysical field enhancements and the associated difficulty in reaching convergence, results have been omitted for nanocups with core offsets of  $D = 1 - 1.4$ .

Far-field extinction spectra were obtained by summing the far field absorption ( $Q_{abs}$ ) and scattering ( $Q_{scat}$ ) efficiencies. Scattering spectra were calculated on a spherical boundary as:

$$Q_{scat} = \frac{1}{\pi \cdot r_2^2 \cdot E_{inc}^2} \frac{1}{R_f^2} \int |\mathbf{E}_{far}|^2 \cdot R_f^2 \cdot d\Omega \quad (2.1)$$

where  $R_f$  is the radius of the boundary used for calculating the far-field transform,  $\mathbf{E}_{far}$  is the vectorial far-field component of the scattered field calculated with the COMSOL implementation of the Stratton-Chu formula [33], and  $E_{inc}$  is the incident electric field amplitude. The factor of  $R_f^2$  inside the integral is introduced automatically by COMSOL as a normalization factor during the boundary integration and must be removed during post-processing to obtain the correct magnitude of  $Q_{scat}$ . Absorption efficiencies were determined similarly by integrating the time averaged resistive heating ( $U_{av}$ ):

$$Q_{abs} = \frac{1}{\pi \cdot r_2^2} \frac{2}{\sqrt{\epsilon_0 / \mu_0} E_{inc}^2} \int (U_{av}) \cdot dV \quad (2.2)$$

Near field enhancements at a point  $p$  are defined as the total electric field amplitude ( $E_{tot}$ ) at the nanoparticle surface normalized to the incident field magnitude

$(\eta_p = E_{tot} / E_{inc})$  where, on resonance, the total electric field near the particle surface is dominated by scattering ( $E_{tot} + E_{scat} \approx E_{scat}$ ). In the context of this study, the enhancement is determined by taking the average of the ten largest scattered field elements above the nanoparticle surface. Spectral peak wavelengths and amplitudes were determined using a custom analysis code in conjunction with a cubic spline interpolating function to reduce granularity in the calculated spectra.

The computational cost of calculating scattering and absorption spectra for a given geometry was significant, with a single particle geometry requiring 5-10 hours using the PARDISO direct solver with shared memory parallelism enabled. Simulations for multiple geometries were performed in parallel on multiple 64-bit compute nodes, each with 16 GB of RAM and eight 2.83 GHz Intel® Xeon® cores. Desktop workstations performing these same calculations, using 64-bit single- or dual-core processors and 8 GB of RAM, required 4-8 times longer.

### 2.3 Far field spectra of nanoparticles

The far field spectra of  $[r_1, r_2] = [30, 35]$  nm nanoshells, nanoeggs, and nanocups as a function of core offset parameter  $D$ , along with their associated multipolar resonances, are shown in Figure 2.2. For nanoshells ( $D = 0$ ) the FEM and Mie calculations agree with each other (Figure 2.2(a)). For core offsets ranging from  $0 < D < 0.32$ , the spectra continue to closely resemble that of a nanoshell. As  $D$  is increased beyond that range, several multipolar peaks begin to appear, subsequently redshifting with increasing core offset. Once the core pierces through the shell, forming a nanocup, the spectrum is similar but shifted to even longer wavelengths. Additional increases in  $D$  beyond this

point, as the core moves further outside the shell, cause the peaks to blueshift until they are resonant with the interband transitions of Au and are damped. Qualitatively similar spectral properties were obtained for [45, 52.5] nm and [60, 70] nm radii particles, indicating that the trends observed here are quite general for particles beyond the quasistatic regime.

The formation of multipolar spectra when  $D \approx 1$  for both nanoeggs and nanocups can be understood simply as the mixing, or hybridization, of primitive sphere and core plasmons. For nanoeggs in the quasistatic regime, plasmon hybridization has produced an analytical method of calculating plasmon modes [34]; however, no such method yet exists for nanocups. The plasmon hybridization picture, however, allows us to develop a physical understanding of the calculated resonances without the need for an explicit solution [35-37].

In the spherically symmetric case, multipoles of the primitive plasmon modes can interact only with modes of the same angular momentum index: dipolar sphere modes hybridize only with dipolar cavity modes, for example. With the reduced symmetry of nanoeggs, this selection rule is relaxed and the multipolar primitive sphere plasmon modes, for example, can hybridize with all multipolar cavity plasmon modes. The resulting hybridized energy levels can then contain elements of the many multipolar modes. As  $D \rightarrow 1$ , an increasing number of optically active modes appear, and the modes redshift, even in the quasistatic limit, due to the increased interaction between primitive plasmon modes. Following previous notation, these mixed mode resonances are labeled using the multipolar index  $l$  corresponding to the orthogonal modes of a symmetric nanoshell [26].

For nanocups ( $D > 1$ ), the pure cavity and sphere hybridization model no longer applies. However, due to geometry and different dielectric embedding media, there are distinct plasmons associated with the cavity inside the cup, which is in contact with silica, and the outer surface of the shell, which is in contact with air. As with nanoeggs, these two primitive plasmons hybridize and form mixed mode resonances which may also be referred to using the multipolar index  $l$ . As  $D$  increases, and the core moves further outside of the shell, the primitive plasmon modes hybridize more weakly, resulting in a subsequent blueshift of the multipolar modes. Nanocup modes without strong inherent dipolar components, such as the  $l = 4$  and  $l = 3$  peaks, weaken and vanish as  $D \rightarrow \infty$  since they can only be excited in the case of strong hybridization.

These results show strong similarity to previous work by Cortie and Ford [7], which included the calculated extinction spectra of a [35, 50] nm radii nanocup with flat edges. A quantitative comparison between their semi-shell nanocup geometry and the offset-core geometry reported here is not possible due to differing sizes, core-shell aspect ratios, and embedding media. However, they do observe a strong resonance (which they denote as  $\alpha$ ) at 610 nm for light polarized parallel to the cup's axis of symmetry, which corresponds to the dipole-active  $l = 3$  multipolar resonance of the offset-core nanocups. As Cortie and Ford decrease the cutoff height of the semi-shell, which is analogous to increasing  $D$ , they observe a blueshifting and weakening of this resonance in agreement with Figure 2.2.

The two weakest, and most redshifted, plasmon resonances for nanocups (Figure 2.2(b)) have not been observed in previous experiments [24, 27]. The absence of these peaks could be partially due to modification of the bulk dielectric function by size-



dependent electron scattering for large core-shell offsets [38], as the electron mean free path may be significantly reduced due to shell thinning, which would weaken and broaden plasmon peaks while leaving the peak wavelengths essentially unchanged [7, 39, 40]. However, whether or not the bulk dielectric function needs to be modified is controversial. Single particle spectroscopic measurements of nanoshells correlated with Mie theory suggest that inhomogeneous broadening may be the dominant factor in plasmon linewidth broadening, not deviations from the bulk dielectric function [41].

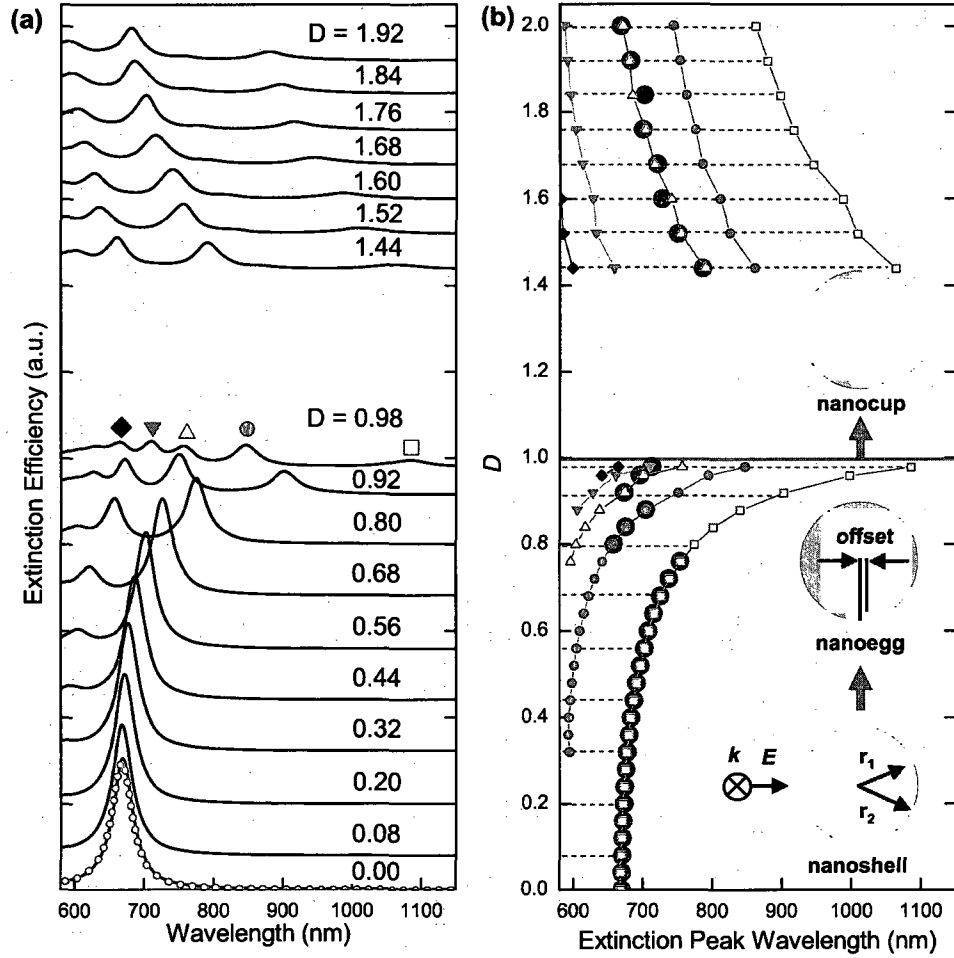


**Figure 2.2.** Far field extinction properties of  $[r_1, r_2] = [30, 35]$  nm nanoeggs and nanocups composed of a gold shell surrounding a silica core with displacement  $D = \text{offset}/(r_2 - r_1)$ . (a) Extinction spectra for a plane wave polarized as indicated in diagram (spectra offset for clarity). Black lines were calculated using FEM; red dots overlaid on the  $D = 0$  spectra are the corresponding Mie theory result. (b) Peak wavelengths of multipolar extinction spectra shown in (a). Colored lines indicate peak wavelengths (red squares,  $l = 1$ ; green circles,  $l = 2$ ; pink triangles,  $l = 3$ ; light blue inverted triangles,  $l = 4$ ; dark purple diamonds,  $l = 5$ ). Gray circles denote wavelength of maximum E-field enhancement.

## 2.4 Nanoegg near field properties

Changing of the core offset  $D$  causes significant changes in both the spatial volume and intensity of the enhanced near fields of the nanoegg structure (Figure 2.3). The near field focusing of a nanoegg can be increased in two ways: offsetting the core and, for a given core offset, exciting the nanoegg at a higher-energy multipolar resonance.

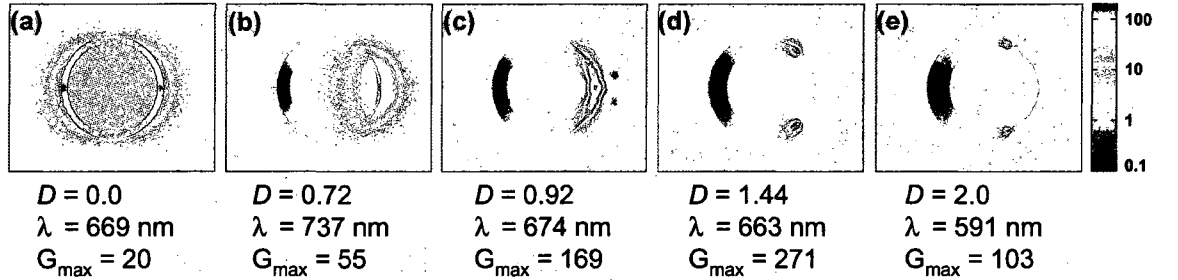


**Figure 2.3.** Local field enhancements of a [30, 35] nm radii (a) nanoshell, (b-c) nanoeggs, and (d-e) nanocups as a function of core offset.

Increasing the core offset causes more intense focusing of the  $l=1$  peak. Higher energy hybridized modes will also increase the field enhancement, as shown in the near field plots in Figure 2.4(a-d), calculated at the four extinction peaks. For all plasmon resonances, enhancement occurs on the outer shell surface and is strongest on the thinnest part of the nanoegg.

Field enhancements at the  $l=1$  peak, along with the maximum field enhancement attainable for a given nanoegg core offset, are shown in Figure 2.4(f) for three sizes of nanoegg with identical core-shell ratios. Most experimentally accessible geometries will have  $D=0$  to  $D=0.8$ , where the maximum enhancement occurs at the  $l=1$  peak.

The field enhancements shown in Figure 2.4(f) were independent of meshing, as the continuous layer of gold around the nanoegg core lacks sharp edges or discontinuities in

the simulation space. Enhancements for nanocups are not reported, however, since the sharp tips that result from a simple core-offset model produce unphysical field enhancements (up to 700) with a strong dependence on meshing parameters. Spectra for the cups reported here do show good qualitative agreement with previously reported cup structures without sharp tips [7, 27], suggesting that their far field properties are not completely dominated by tip effects. For both structures the field enhancements may be significantly affected by the surface roughness and shell defects inherent to chemically synthesized particles [7, 30].

The difference between the wavelength of maximum field enhancement and the extinction wavelength for the mixed  $l=1$  mode ( $\Delta\lambda = \lambda_{G\max}^{l=1} - \lambda_{Gext}^{l=1}$ ) is shown in Figure 2.4(g). For nanoshells it is well known that the maximum field enhancement is always redshifted relative to the extinction peak [42]. For nanocups, the enhancement peak blueshifts relative to the extinction peak as  $D$  increases. This offset is more significant for larger nanoeggs, and could prove critical when designing nanoeggs with a desired field enhancement maximum.

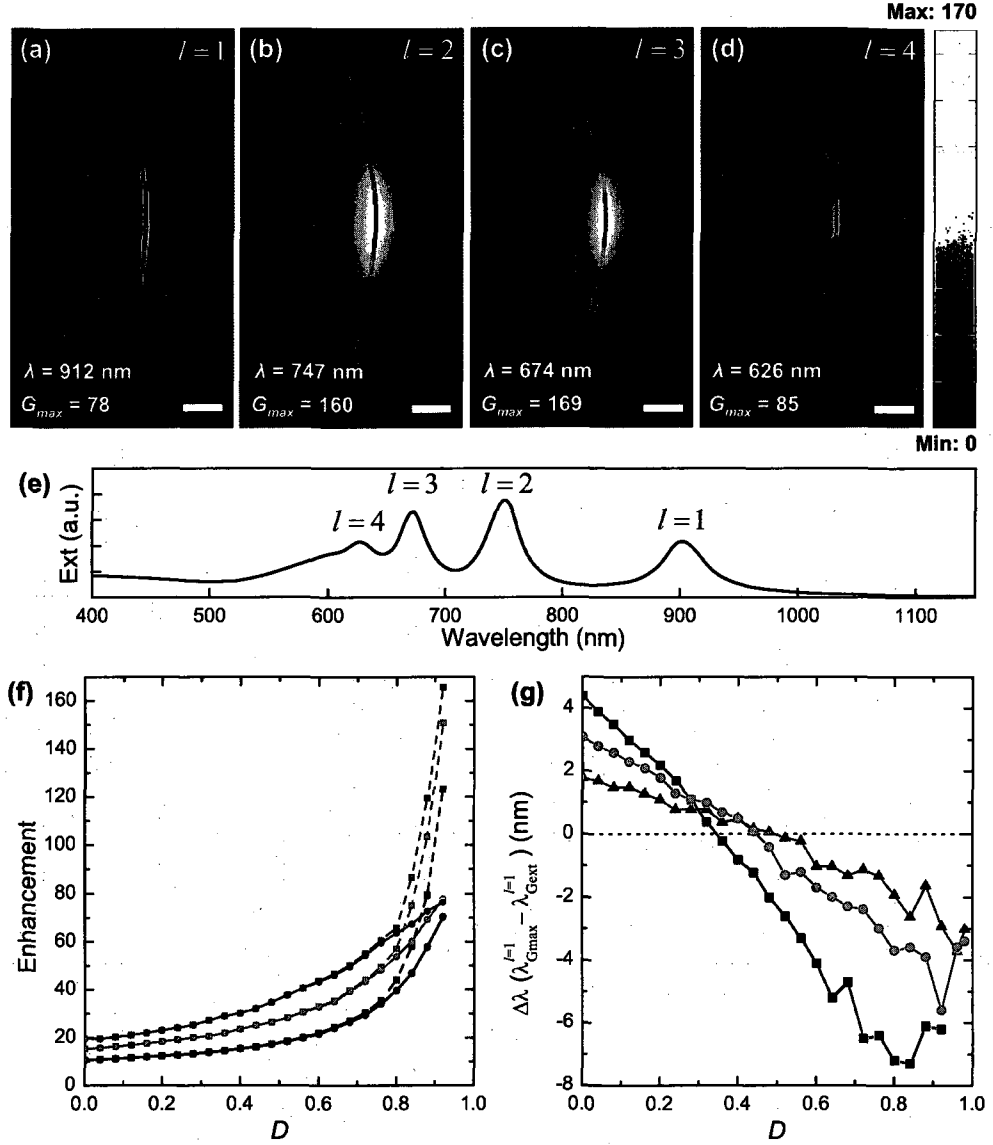


**Figure 2.4.** Local field enhancement properties of nanoeggs as a function of core offset. (a-d) Field enhancements ( $G$ ) of a [30, 35] nm nanoegg with a 4.6 nm core offset ( $D = 0.92$ ) at the four scattering peaks. Scale bars are 2 nm. (e) Far-field extinction spectra corresponding to field enhancement plots. (f) Comparison between the maximum E-field enhancement at the dipole scattering peak ( $G_{ext}^{l=1}$ , solid lines) and the maximum enhancement calculated within the entire spectrum for each offset ( $G_{max}$ , dashed lines). Red – [30,35] nm, green – [45,52.5] nm, blue – [60,70] nm. (g) Blueshifting of E-field enhancement peak compared to the extinction peak for the  $l=1$  mixed mode.

## 2.5 Tuning relative absorption and scattering efficiencies

In the quasistatic regime the extinction spectrum of nanoparticles is dominated by absorption; larger particles tend to be dominated by scattering [43]. Controlling the relative magnitudes of absorption and scattering will facilitate further optimization of nanoparticles for use in the NIR.

Absorption and scattering efficiencies for three core-offset nanoparticles calculated at their  $l = 1$  extinction peak are shown in Figure 2.5. In panel (a) the absorption and scattering efficiencies of a quasistatic [30, 35] nm nanoegg decrease as the core is offset, and then increase slowly after the core pierces the shell to form a nanocup. Panel (b) shows a larger, [45, 52.5] nm particle. While absorption still slightly dominates when  $D = 0$ , increasing offsets increase the absorption efficiency slightly until  $D > 0.5$ . Panel (c) shows that an even larger [60, 70] nm nanoegg, solidly beyond the quasistatic limit and dominated by scattering when  $D = 0$ , can have a dipole extinction peak dominated by absorption for sufficiently large offsets.

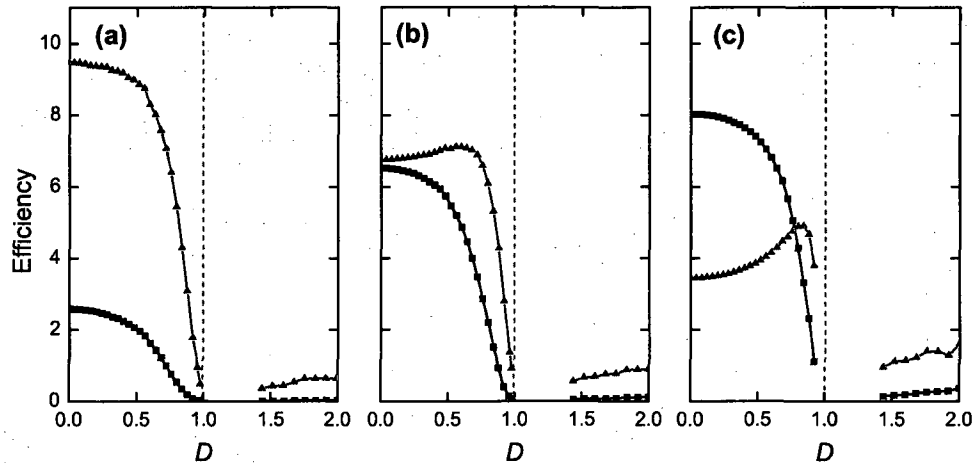


**Figure 2.5.** Comparison of far-field absorption (red triangles) and scattering (black squares) efficiencies at the dipole peak for (a) [30,35] nm nanoegg and nanocup, (b) [45,52.5] nm nanoegg and nanocup, and (c) [60,70] nm nanoegg and nanocup. The incident wave was polarized along the axis of offset, as shown in Figure 2.2.

## 2.6 Concluding remarks

Much as lenses can be used to focus light onto an object of interest, nanoeggs may be viewed as tunable nanoscale optical lenses that can be used to illuminate a molecule or molecules of interest for surface enhanced spectroscopies. Just as one must select a lens with the correct properties, a nanoparticle lens must be designed to focus light into a hotspot matched to the size of the molecule, or group of molecules, of interest. The varying degrees of hotspot confinement corresponding to both offset and multipolar order show that a nanoegg functions as a highly chromatic nanolens, with the volume of the enhanced field associated with each multipolar resonance optimized for different sizes of analyte.

This chapter has shown that controlled tuning of the nanoparticle plasmon behavior is possible by varying the core offset parameter  $D$ , and by choosing which multipolar resonances should be excited. Taking into account the relative blueshift between the  $l = 1$  enhancement and extinction peaks could prove critical to further optimization of nanoeggs as active SERS substrates.

For applications where absorption is a desirable property, small nanoshells with their tunable plasmon frequency and strong absorption characteristics are ideal. If a larger particle is required or dictated by the available chemical synthesis methods, the relative contribution of absorption to the extinction spectrum can be increased by offsetting the particle core. Such offsets could be achieved experimentally by electroless plating [26] or evaporation onto spherical templates [21].

For medical imaging applications, where scattering is desirable, large symmetric nanoshells give significantly larger signals than either gold nanoparticles, or asymmetric

structures such as nanoeegs, cups, or rods [44]. These results suggest that an admixture of large nanoshells, for imaging, and tuneable absorbers such as nanorods or nanoeegs, for photothermal therapy, may prove useful for hybrid biomedical imaging and treatment applications requiring both significant absorption and significant scattering [3].



# **Chapter 3: Nanoparticle-mediated Coupling of Light and Nanowire Plasmons**

## **3.1 Introduction**

Coupling light from free space into plasmon waveguides, by compensation of the momentum difference between photons and plasmons, presents a critical challenge. Current methods of optical signal injection into plasmonic waveguides include excitation at waveguide defects [12, 15, 18, 45], bends [18], crossed wire junctions [18, 46, 47], and evanescent wave excitation using the Kretschmann geometry [17, 48]. A new signal injection scheme, first published by Hao and Nordlander, takes advantage of the mixing of adjacent nanostructures plasmon modes [49]. When a metallic nanoparticle is placed in close proximity to a metallic nanowire the resulting “hybridized” plasmon modes [29], where localized plasmons on metallic nanoparticles couple with the propagating plasmons supported by metallic films or wires [50, 51], provide a mechanism for injecting free-space photons into nanowire plasmons at infrared and optical frequencies. The conversion efficiencies should be significantly greater than with direct optical excitation [49]. This spatially compact geometry allows for direct coupling into straight, continuous nanoscale wires and is, therefore, an ideal candidate for photonic input and output ports on dense, integrated plasmonic circuitry.

This chapter will discuss the observation of metallic nanoparticle-mediated coupling of visible light with propagating plasmons in directly adjacent metallic nanowires. Visible light is focused onto individual nanowire-nanoparticle junctions. The plasmon resonance of the interacting nanoparticle-nanowire system provides sufficient coupling of

light into the nanowire, exciting propagating plasmons in the structure. Nanowire plasmons are also converted back to free-space photons at these nanoparticle-nanowire junctions, as well as at kinks and ends of nanowires [18]. This assortment of plasmon launching and scattering sites allows us to examine the relative plasmon coupling efficiencies of these geometries, and also provides probe sites for examining the polarization dependence of plasmon excitation on nanowires of various lengths and conformations, using optical microscopy.

### **3.2 Nanoparticle fabrication and optical characterization**

The crystalline Ag nanowires that serve as waveguides in this study were synthesized using room temperature chemical fabrication, yielding nanowires with a mean diameter of  $\sim 220$  nm and lengths ranging from 1 to 25  $\mu\text{m}$  [52]. Platinum seed was formed by reducing  $\text{PtCl}_2$  with ethylene glycol (EG) at  $160 \pm 3^\circ\text{C}$ , then adding  $\text{AgNO}_3$  and poly(vinyl pyrrolidone) (PVP) dropwise over the course of six minutes. After the  $\text{AgNO}_3$  was completely reduced ( $\sim 60$  minutes), the solution was cooled, washed via centrifugation once in acetone to remove EG, then twice in ethanol to remove PVP. The spherical Ag nanoparticles serving as plasmonic couplers had diameters varying from 200 – 700 nm, and were cofabricated in the same chemical synthesis procedure as the nanowires, remaining in solution with the nanowires following centrifugation.

Samples for these studies were prepared by drop-casting a dilute ethanolic suspension of this Ag nanowire-nanoparticle mixture on glass slides patterned with indexed grids and letting them dry under ambient conditions. A small percentage of the colloidal Ag nanoparticles were observed to deposit within  $\sim 10$  nm of certain Ag

nanowires. To characterize coupling behavior, individual nanowire-nanoparticle junctions were positioned near the intensity maximum of a diffraction-limited laser spot ( $\lambda = 633 \text{ nm}$ ) using a piezoelectric stage (Nanonics Imaging Ltd., 3D Flat Scanner<sup>TM</sup>) mounted on an inverted optical microscope (Zeiss Axiovert 200 MAT) (Figure 3.1). Polarization control of the laser light was achieved using a Glan-Thompson polarizing beamsplitter cube followed by a  $\lambda/2$  plate (multi-order, 633 nm) in a rotation mount. The polarized laser beam was directed into the microscope using a half-silvered mirror and focused to a diffraction-limited spot in the image plane using a 100x objective lens (Zeiss, N.A. = 0.9). Light scattered from the sample passed through a half-silvered mirror and was detected using a CCD (Axiocam MRm,  $1388 \times 1040 \text{ px}$ , spectral range: 350 – 1000 nm). Rotating the  $\lambda/2$  plate before recording each far-field image allowed the construction of curves showing relative far-field intensity as a function of laser polarization angle. High resolution images of the individual nanowire-nanoparticle pairs were obtained using scanning electron microscopy (SEM, FEI Quanta 400).

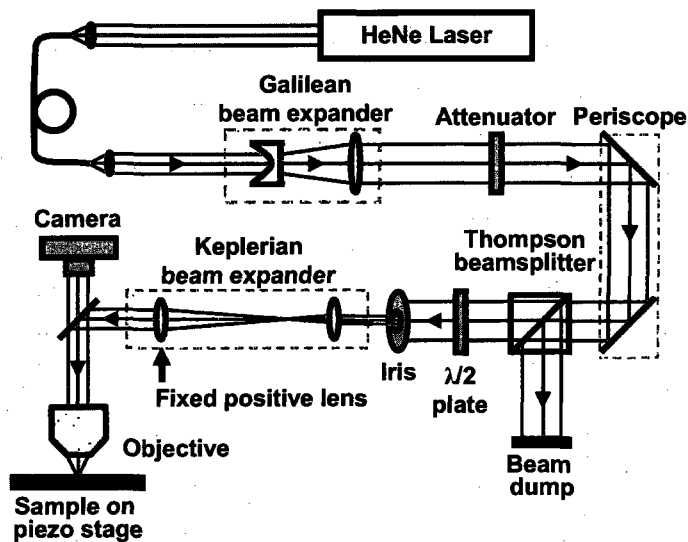


**Figure 3.1.** Optical layout used for nanowire excitation and remote emission measurements. The fixed positive lens in the Keplerian beam expander was located inside the Zeiss microscope and could not be adjusted.

### 3.3 Demonstration of Polarization Dependent Coupling

In Figure 3.2, an individual nanowire with an adjacent Ag nanoparticle allows us to examine nanoparticle-nanowire coupling, as well as other input and output coupling mechanisms, all in a single nanostructure complex. In Figure 3.2(A), the nanoparticle-nanowire junction is illuminated with a diffraction-limited beam spot, and emission can be observed from the nanowire terminus closest to the excitation junction. The wire plasmon wavelength in this sample was found to be  $440 \pm 5$  nm, measured by collection-mode near-field scanning optical microscopy. Previous measurements have reported decay lengths for nanowire plasmons on similar structures of 3-10  $\mu\text{m}$  [16, 18, 53], a length scale consistent with the observation of emission only at the nearest nanowire terminus to the plasmon launch site. When the launch geometry is reversed, that is, end-on illumination of the nanowire, emission is observed at the nanoparticle-nanowire coupling site (Figure 3.2(B)). A kink in the nanowire can also serve as a coupling site for nanowire plasmon excitation (Figure 3.2(C)), and emission (Figure 3.2(D)). In this specific example, the kink in the nanowire consisted of two bends, separated by 900 nm, with angles of  $136^\circ$  and  $147^\circ$  (Figure 3.3(A)). The associated dipole moment can be anticipated to be weak relative to end- or particle-coupling geometries, and indeed, it was observed that higher laser excitation powers were necessary for exciting observable remote emission from the kink relative to either the nanoparticle or end-on coupling geometries.

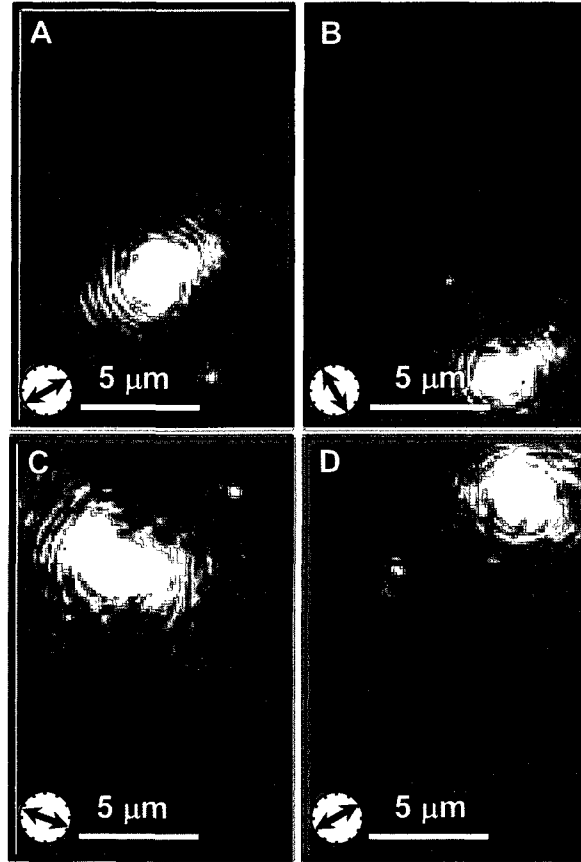


**Figure 3.2.** Optical images obtained in bright field microscopy showing coupling between free-space photons and nanowire plasmons at multiple points of broken symmetry. The focused laser spot was used to excite propagating wire plasmons by illumination at (A) a 216 nm diameter metallic particle adjacent to the nanowires, (B) the end of the nanowire, (C) the kink in the nanowire, and (D) the alternate end of the nanowire. Red arrows indicate the laser spot polarization corresponding to maximum nanowire plasmon emission.

Coupling strength was measured by illuminating the particle-wire junction with a linearly polarized, diffraction-limited laser spot (Figure 3.3). For each polarization an emission intensity for a given coupling site was determined by averaging the three brightest pixels at that site; small variations in reflectance coefficients for TE and TM polarizations were corrected for numerically. Data were obtained for multiple orientations of the same wire relative to the microscope, to ensure that the calibrated intensity curves resulted from the coupling geometries, and were not generated as artifacts of the optical setup. The 16.67  $\mu\text{m}$  wire shown in Figure 3.3 was excited at the

nanowire-nanoparticle junction (Figure 3.3(A), site *b*), with observations recorded at the three remote coupling sites (*a*, *c*, and *d*). Data was taken using low power for site *a* to avoid saturating the detector; a second dataset was taken with higher power levels to improve the signal/noise ratio for the weaker emission observed at sites *c* and *d*. Figure 3.3(B) shows that coupling maxima and minima correspond to laser polarizations perpendicular and parallel to the wire, respectively. The polarization dependence corresponding to the maximum plasmon emission at the remote sampling sites on the nanowire is in agreement with theory, which predicts maximum coupling for light polarized across the nanoparticle wire junction [49]. Far-field emission curves from remote sites as a function of polarization angle are well described by a simple sinusoidal dependence,

$$I(\theta) = I_0 \cos(2\theta + \phi_{phase}) + I_{offset} \quad (3.1)$$

with a period of  $180^\circ$  and maxima at  $\phi_{phase}$  (Figure 3.3(B)) (here  $I_{offset}$  is a fit parameter that scales the mean intensity averaged over all measured polarizations). It is interesting to note the shift in polarization for the distal end (site *d*) coupling peak polarization, to  $102 \pm 4^\circ$ , from the coupling maxima observed at the other emission sites.

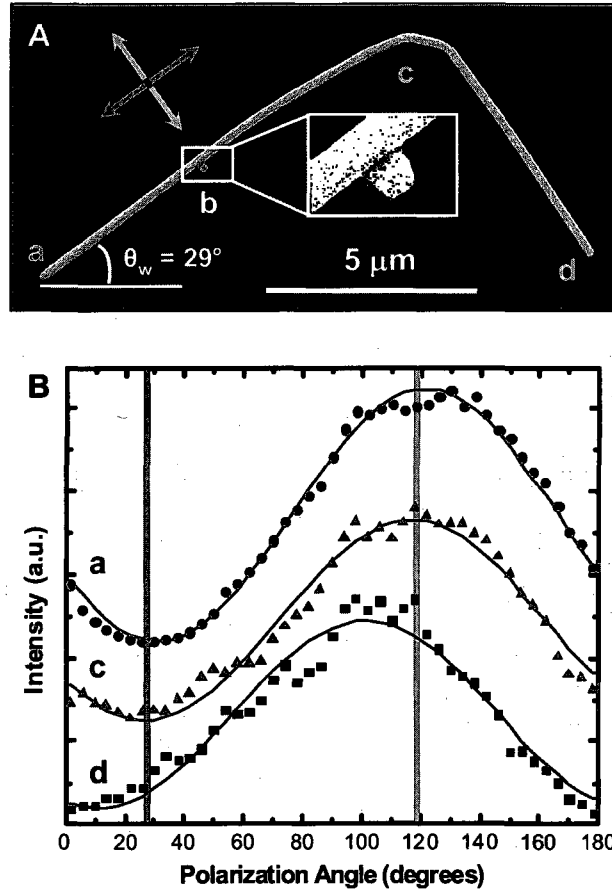


**Figure 3.3.** Polarization-dependence of coupling efficiency at nanoparticle-wire junction. (A) SEM of silver nanoparticle (critical dimension = 216 nm) adjacent to a bent silver nanowire (length = 16.65  $\mu\text{m}$ , width = 222 nm). Propagating plasmons were excited at the wire-particle junction (b) by a diffraction-limited laser spot ( $\lambda = 633 \text{ nm}$ ). (B) Far-field emission intensities as a function of laser polarization angle (normalized and vertically offset for clarity). Strongest coupling observed for polarization perpendicular to the wire (light blue); weakest coupling occurs when polarization is parallel to the wire (purple). Black lines are best-fit sine curves.

For shorter nanowires, the polarization dependence of the far-field nanowire plasmon emission was found to be highly sensitive to junction position and nanowire length. Nanowires and nanoparticle-nanowire junctions were measured with various degrees of oxide coatings that appeared subsequent to sample preparation; however, it is important to note that this oxidation of the nanowire-nanoparticle junction structures was found to have negligible effect on optical coupling properties (Figure 3.4(A, B)). In Figure 3.4(C), end-excitation of nanowire plasmons with emission from both the centrally positioned

nanoparticle-nanowire junction as well as emission from the opposite end of the nanowire are shown. In Figure 3.4(D), the central nanoparticle-nanowire junction is illuminated, resulting in emission from both ends of the nanowire. In each of these two excitation geometries the relative polarization dependence of the two plasmon “output ports” of the nanostructure is observed. Figure 3.4(E) shows the polarization dependence of the two emission sites of the excitation geometry for the nanostructure shown in Figure 3.4(C), while in Figure 3.4(F) the polarization dependence corresponding to the structure and excitation geometry of Figure 3.4(D) are displayed.



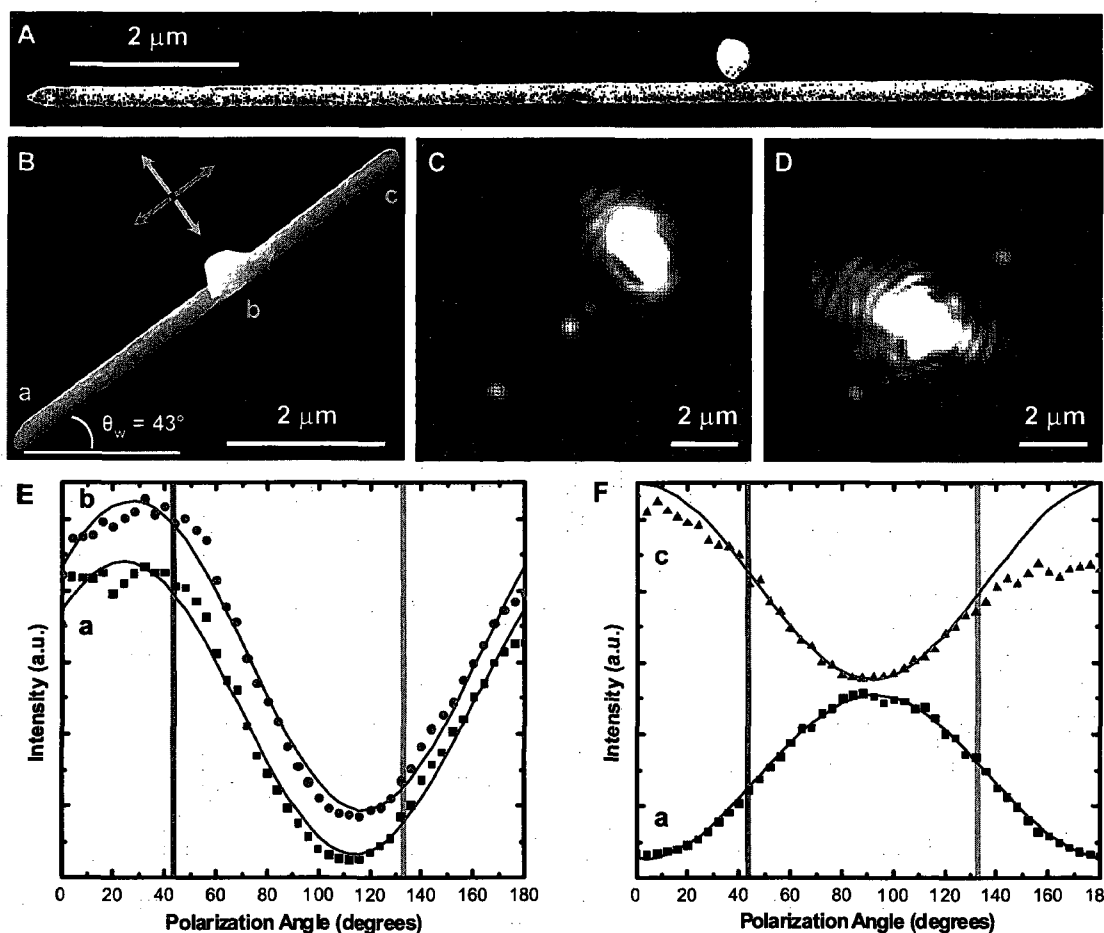


**Figure 3.4.** Geometry dependence of polarization angle for maximum far-field emission intensity (normalized and offset for clarity). (A) SEM of representative coupled silver nanoparticle-wire pair prior to environmental oxidation. (B) SEM of wire used in (C)–(F). Wire length = 5.96 μm, diameter = 259 nm, particle diameter = 660 nm. (C) Optical images of light coupled into nanowire through end of nanowire and (D) nanowire/nanoparticle junction. (E) Emission intensities from remote coupling sites (*a*) and (*b*) when illuminated at end of nanowire (*c*). (F) Emission intensities from (*a*) and (*c*) when illuminated at nanowire-nanoparticle junction (*b*). Black lines are best-fit sine curves.

### 3.4. Theoretical Model

Finite element analysis simulations using commercial software (COMSOL Multiphysics) were used to study both excitation geometries shown in Figure 3.4(C, D) using an approach similar to that presented in Section 2.2. Briefly, the nanowire and nanoparticle were modeled using a simple rod and sphere of the same dimensions as the nanowire-

nanoparticle pair shown in Figure 3.4(B), surrounded by a cylindrical simulation space with scattering boundaries on the outer surface. A polarized, Gaussian beam (beam waist = 2  $\mu\text{m}$ ) was simulated as the excitation source (Figures 3.5(A) and 3.5(B)). For a given source polarization, the emission intensities of remote sites were calculated by applying far-field transforms to the wire at each point of broken symmetry. The theoretical emission curves were normalized for comparison to experimental measurements. In this study it was found that varying the wire length by less than 40 nm can drastically alter the relative polarization dependence of the observed emission. This dramatic effect may quite possibly be due to short nanowires functioning as Fabry-Pérot cavities with end-face reflectivities of  $\sim 25\%$  [16, 53], where resonant modes are selected by the laser polarization angle. The experimental and theoretical peaks agree to within  $20^\circ$  or less, where the discrepancy is likely due to uncertainties in the exact dimensions of the physical nanowire and placement of the nanoparticle (surface oxide coating the nanoparticle and nanowire limited the measurement accuracy of system dimensions). Experimentally, this interpretation is supported by the observation that plasmons launched from wire ends always yield remote emission curves with maxima and minima corresponding to polarizations aligned longitudinally and transverse to the nanowire, respectively. This is the expected behavior for a coupling modality with a fixed plasmon launching phase (Figure 3.4(E)). Also in agreement with the Fabry-Pérot cavity interpretation, emission peak offsets disappear for long wires since Ohmic losses decrease the amplitude of the interfering plasmons.

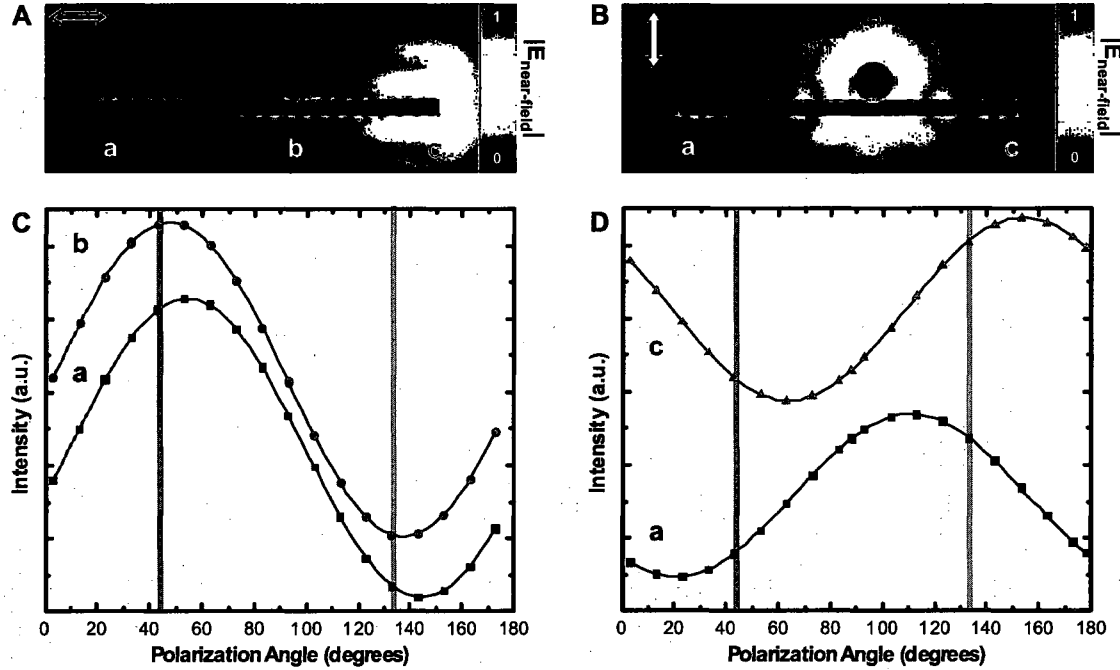


**Figure 3.5.** Finite element analysis of nanoparticle-wire geometry shown in Figure 3.4(B). (A) Near-field amplitude of electric field for end excitation with polarization along wire (purple) and (B) particle excitation with polarization perpendicular to wire (light blue). (C) Emission intensities from remote coupling sites (*a*) and (*b*) when illuminated at end of wire, and (D) Emission intensities from sites (*a*) and (*c*) when illuminated at the nanoparticle-wire junction. Black lines are best-fit sine curves.

### 3.5 Concluding remarks

In this chapter I have demonstrated that plasmons can be launched on nanowires using a directly adjacent particle nanoantenna. Emission amplitudes from remote coupling sites depend strongly on polarization for all wire lengths. For long wires (length  $> 10 \mu\text{m}$ ) plasmon emission at the ends of the nanowire is strongly polarization dependent, with maximum emission corresponding to polarization transverse to the nanowire axis. Short nanowire far-field emission is highly dependent on the specific nanowire/nanoparticle geometry observed.

This nanoparticle-mediated plasmon coupling geometry may ultimately prove to be ideal for optical input and output ports on dense, integrated plasmonic circuitry, and

could allow the further development of nanoscale plasmon-based interferometers and other standing wave plasmon-based passive or active optical components.

## Chapter 4: Summary

This thesis has examined the effects of breaking symmetry on two structures with significant technological importance – nanoshells and nanowires – using FEM models and, for nanowires, experimental realization of the system.

The simulation method used to study these two structures generalizes to other materials and geometries, and provides a simple route to understanding the optical behavior of particles with arbitrary geometries and complex multiparticle structures. The rapid development of multicore processors, and the integration of additional RAM into desktop machines, will continue to increase the ease with which such models can be used and allow future work in experimental plasmonics to be rapidly compared with electrodynamics modeling.

In the case of nanoeggs and nanocups it has been shown that the core offset can be used to design a highly chromatic ‘plasmonic nanolens’ with near-field enhancements and confinement significantly greater than what can be obtained with an equivalent symmetric nanoshell. Changing the core offset also permits substantial tuning of the far-field properties, including resonance peak wavelengths and the ratio of absorption to scattering. For nanowires, breaking symmetry by the addition of a vicinal nanoparticle antenna allows the polarization-controlled launch of wire plasmons.

These observations may lead to technological improvements in cancer therapy, medical imaging, spectroscopy, high-speed computation, or inspire the development of future active plasmonic devices exploiting the effects of broken symmetry.

## References

- [1] S. Lal, S. Link, and N. J. Halas, "Nano-optics from sensing to waveguiding," *Nature Photonics* **1**, 641-648 (2007).
- [2] A. M. Gobin, M. H. Lee, N. J. Halas, W. D. James, R. A. Drezek, and J. L. West, "Near-infrared resonant nanoshells for combined optical imaging and photothermal cancer therapy," *Nano Lett.* **7**(7), 1929-1934 (2007).
- [3] C. Loo, A. Lin, L. Hirsch, M.-H. Lee, J. Barton, N. Halas, J. West, and R. Drezek, "Nanoshell-Enabled Photonics-Based Imaging and Therapy of Cancer," *Technol. Cancer Res. Treat.* **3**(1), 33-40 (2004).
- [4] S. Oldenburg, S. Westcott, R. D. Averitt, and N. J. Halas, "Surface enhanced Raman scattering in the near infrared using metal nanoshell substrates," *J. Chem. Phys.* **111**(10), 4729-4735 (1999).
- [5] C. L. Haynes, A. D. McFarland, and R. P. Van Duyne, "Surface-enhanced Raman spectroscopy," *Anal. Chem.* **77**, 338A-346A (2005).
- [6] D. R. Ward, N. K. Grady, C. S. Levin, N. J. Halas, Y. Wu, P. Nordlander, and D. Natelson, "Electromigrated nanoscale gaps for surface-enhanced Raman spectroscopy," *Nano Lett.* **7**(5), 1396-1400 (2007).
- [7] M. Cortie and M. Ford, "A plasmon-induced current loop in gold semi-shells," *Nanotechnology* **18**, 235704 (2007).
- [8] E. Ozbay, "Plasmonics: Merging photonics and electronics at nanoscale dimensions," *Science* **311**(5758), 189-193 (2006).
- [9] M. J. Kobrinsky, B. A. Block, J.-F. Zheng, B. C. Barnett, E. Mohammed, M. Reshotko, F. Robertson, S. List, I. Young, and K. Cadien, "On-Chip Optical Interconnects," *Intel Technol. J.* **8**(2), 129-143 (2004).
- [10] S. A. Maier, M. D. Friedman, P. E. Barclay, and O. Painter, "Experimental demonstration of fiber-accessible metal nanoparticle plasmon waveguides for planar energy guiding and sensing," *Appl. Phys. Lett.* **86**, 071103 (2005).
- [11] D. Qu and D. Grischkowsky, "Observation of a new type of THz resonance of surface plasmons propagating on metal-film hole arrays," *Phys. Rev. Lett.* **93**(19), 196804 (2004).
- [12] D. F. P. Pile and D. K. Gramotnev, "Channel plasmon-polariton in a triangular groove on a metal surface," *Opt. Lett.* **29**(10), 1069-1071 (2004).

- [13] S. I. Bozhevolnyi, V. S. Volkov, E. Devaux, J. Y. Laluet, and T. W. Ebbesen, "Channel plasmon subwavelength waveguide components including interferometers and ring resonators," *Nature* **440**(7083), 508-511 (2006).
- [14] B. Lamprecht, J. R. Krenn, G. Schider, H. Ditlbacher, M. Salerno, N. Felidj, A. Leitner, F. R. Aussenegg, and J. C. Weeber, "Surface plasmon propagation in microscale metal stripes," *Appl. Phys. Lett.* **79**(1), 51-53 (2001).
- [15] A. Graff, D. Wagner, H. Ditlbacher, and U. Kreibig, "Silver nanowires," *Europ. Phys. J. D* **34**, 263-269 (2005).
- [16] H. Ditlbacher, A. Hohenau, D. Wagner, U. Kreibig, M. Rogers, F. Hofer, F. R. Aussenegg, and J. R. Krenn, "Silver nanowires as surface plasmon resonators," *Phys. Rev. Lett.* **95**25(25), 257403 (2005).
- [17] J. R. Krenn and J. C. Weeber, "Surface plasmon polaritons in metal stripes and wires," *Phil. Trans. A* **362**(1817), 739-756 (2004).
- [18] A. W. Sanders, D. A. Routenberg, B. J. Wiley, Y. N. Xia, E. R. Dufresne, and M. A. Reed, "Observation of plasmon propagation, redirection, and fan-out in silver nanowires," *Nano Lett.* **6**(8), 1822-1826 (2006).
- [19] M. W. Knight and N. J. Halas, "Nanoshells to Nanoeggs to Nanocups," *New J. Phys.* **ASAP** (2008).
- [20] M. W. Knight, N. K. Grady, R. Bardhan, F. Hao, P. Nordlander, and N. J. Halas, "Nanoparticle-Mediated Coupling of Light into a Nanowire," *Nano Lett.* **7**(8), 2346-2350 (2007).
- [21] H. Takei, "Surface-adsorbed polystyrene spheres as a template for nanosized metal particle formation: Optical properties of nanosized Au particle," *J. Vac. Sci. Tech. B* **17**, 1906 (1999).
- [22] H. Takei, M. Himmelhaus, and T. Okamoto, "Absorption spectrum of surface-bound cap-shaped gold particles," *Opt Lett.* **27**(5), 342-344 (2002).
- [23] J. Liu, B. Cankurtaran, G. Mccredie, M. Ford, L. Wieczorek, and M. Cortie, "Investigation of the optical properties of hollow aluminium 'nano-caps'," *Nanotechnology* **16**(12), 3023-3028 (2005).
- [24] J. Liu, A. I. Maarouf, L. Wieczorek, and M. Cortie, "Fabrication of hollow metal 'nanocaps' and their red-shifted optical absorption spectra," *Adv. Mater.* **17**, 1276-1281 (2005).

- [25] J. Liu, B. Cankurtaran, L. Wieczorek, M. Ford, and M. Cortie, "Anisotropic Optical Properties of Semitransparent Coatings of Gold Nanocaps," *Adv. Funct. Mater.* **16**(11), 1457-1461 (2006).
- [26] H. Wang, Y. Wu, B. Lassiter, C. L. Nehl, J. H. Hafner, P. Nordlander, and N. J. Halas, "Symmetry breaking in individual plasmonic nanoparticles," presented at the Proc. Natl. Acad. Sci. U.S.A., Jul 18, 2006.
- [27] C. Charnay, A. Lee, S. Q. Man, C. E. Moran, C. Radloff, R. K. Bradley, and N. J. Halas, "Reduced symmetry metallodielectric nanoparticles: chemical synthesis and plasmonic properties," *J. Phys. Chem. B* **107**, 7327-7333 (2003).
- [28] G. Mie, "Beitrage zur Optik truber Medien, speziell kolloidaler Metallosungen," *Ann. Phys.* **25**, 377-445 (1908).
- [29] E. Prodan, C. Radloff, N. J. Halas, and P. Nordlander, "A hybridization model for the plasmon response of complex nanostructures," *Science* **302**(5644), 419-422 (2003).
- [30] C. Oubre and P. Nordlander, "Optical properties of metallodielectric nanostructures calculated using the finite difference time domain method," *J. Phys. Chem. B* **108**(46), 17740-17747 (2004).
- [31] P. Johnson and R. Christy, "Optical Constants of the Noble Metals," *Phys. Rev. B* **6**(12), 4370-4379 (1972).
- [32] J. Jin, *The Finite Element Method in Electromagnetics (2nd Ed.)* (Wiley-IEEE Press, New York, 2002).
- [33] J. Stratton, *Electromagnetic Theory* (McGraw-Hill, New York, 1941).
- [34] Y. Wu and P. Nordlander, "Plasmon hybridization in nanoshells with a nonconcentric core," *J. Chem. Phys.* **125**(12), 124708 (2006).
- [35] F. Hao, P. Nordlander, M. T. Burnett, and S. A. Maier, "Enhanced tunability and linewidth sharpening of plasmon resonances in hybridized metallic ring/disk nanocavities," *Phys. Rev. B* **76**(24), 245417 (2007).
- [36] F. Hao, C. L. Nehl, J. H. Hafner, and P. Nordlander, "Plasmon resonances of a gold nanostar," *Nano Lett.* **7**(3), 729-732 (2007).
- [37] F. Hao, E. Larsson, T. Ali, D. Sutherland, and P. Nordlander, "Shedding light on dark plasmons in gold nanorings," *Chem. Phys. Lett.* **458**(4-6), 262-266 (2008).
- [38] M. Hu, C. Novo, A. Funston, H. Wang, H. Staleva, S. Zou, P. Mulvaney, Y. Xia, and G. Hartland, "Dark-field microscopy studies of single metal nanoparticles:



- understanding the factors that influence the linewidth of the localized surface plasmon resonance," *J. Mat. Chem.* **18**(17), 1949-1960 (2008).
- [39] R. D. Averitt, S. L. Westcott, and N. J. Halas, "Linear optical properties of gold nanoshells," *J. Opt. Soc. Am. B* **16**(10), 1824-1832 (1999).
  - [40] U. Kreibig and M. Vollmer, *Optical Properties of Metal Clusters*, Springer (Springer, New York, 1995).
  - [41] C. L. Nehl, N. K. Grady, G. P. G. Goodrich, F. Tam, N. J. Halas, and J. H. Hafner, "Scattering spectra of single gold nanoshells," *Nano Lett.* **4**(12), 2355-2359 (2004).
  - [42] N. Grady, N. Halas, and P. Nordlander, "Influence of dielectric function properties on the optical response of plasmon resonant metallic nanoparticles," *Chem. Phys. Lett.* **399**(1-3), 167-171 (2004).
  - [43] F. Tam, A. L. Chen, J. Kundu, H. Wang, and N. J. Halas, "Mesoscopic nanoshells: Geometry-dependent plasmon resonances beyond the quasistatic limit," *J. Phys. Chem.* **127**, 204703 (2007).
  - [44] P. K. J. Jain, K. S. Lee, I. H. El-Sayed, and M. A. El-Sayed, "Calculated absorption and scattering properties of gold nanoparticles of different size, shape, and composition: Applications in biological imaging and biomedicine," *J. Phys. Chem. B* **110**, 7238-7248 (2006).
  - [45] N. Féridj, G. Laurent, J. Grand, J. Aubard, G. Lévi, A. Hohenau, F. R. Aussenegg, and J. R. Krenn, "Far-Field Raman Imaging of Short-Wavelength Particle Plasmons on Gold Nanorods," *Plasmonics* **1**(1), 35-39 (2006).
  - [46] J. A. Deibel, K. L. Wang, M. D. Escarra, and D. M. Mittleman, "Enhanced coupling of terahertz radiation to cylindrical wire waveguides," *Opt. Exp.* **14**(1), 279-290 (2006).
  - [47] K. L. Wang and D. M. Mittleman, "Metal wires for terahertz wave guiding," *Nature* **432**(7015), 376-379 (2004).
  - [48] E. Kretschmann, "Determination of optical constants of metals through the stimulation of surface plasma oscillations," *Z. Phys.* **241**, 313-324 (1971).
  - [49] F. Hao and P. Nordlander, "Plasmonic coupling between a metallic nanosphere and a thin metallic wire," *Appl. Phys. Lett.* **89**, 103101 (2006).
  - [50] F. Le, N. Lwin, J. Steele, M. Ka' il, N. Halas, and P. Nordlander, "Plasmons in the metallic nanoparticle-film system as a tunable impurity problem," *Nano Lett.* **5**(10), 2009-2013 (2005).

- [51] H. Wang, D. Brandl, P. Nordlander, and N. J. Halas, "Plasmonic Nanostructures: Artificial Molecules," *Acc. Chem. Res.* **40**, 53-62 (2007).
- [52] Y. Sun, Y. Yin, B. Mayers, T. Herricks, and Y. Xia, "Uniform silver nanowires synthesis by reducing AgNO<sub>3</sub> with ethylene glycol in the presence of seeds and poly(vinyl pyrrolidone)," *Chem. Mater.* **14**(11), 4736-4745 (2002).
- [53] T. Laroche and C. Girard, "Near-field optical properties of single plasmonic nanowires," *Appl. Phys. Lett.* **89**, 257403 (2006).
- [54] J. D. Jackson, *Classical Electrodynamics*, 3rd ed. (John Wiley & Sons, Inc., New York, 1999).

## Appendix A: Defining Custom Dielectrics

Custom dielectrics can be easily entered into COMSOL either through the built-in ‘**Materials/Coefficients Library**’ interface, or entered into a text file and imported. A material library file can be imported into COMSOL by selecting the menu item ‘**Options**’, ‘**Materials/Coefficients Library**’ and selecting ‘**Add Library...**’ The new library will appear in your ‘**Materials**’ list, and can then be loaded as a subdomain property in the ‘**Subdomain Settings**’ dialog box. A materials library file can contain multiple materials, provided the material index  $i$  in each ‘**lib.mat{i}.**’ entry is incremented for each successive material.

Following reference [54], the equations for the real part of the dielectric constant and the conductivity can be found starting from the Maxwell-Ampère equation:

$$\nabla \times \mathbf{H} = \mathbf{J} + \frac{d\mathbf{D}}{dt}. \quad (\text{A.1})$$

Then, assuming Ohm’s Law ( $\mathbf{J} = \sigma \mathbf{E}$ ) and harmonic time dependence

( $\frac{d\mathbf{D}}{dt} = \frac{d(\epsilon_r \mathbf{E})}{dt} = -i\omega \epsilon_r \mathbf{E}$ ), this equation becomes:

$$\nabla \times \mathbf{H} = -i\omega(\epsilon_r + i\frac{\sigma}{\omega})\mathbf{E}, \quad (\text{A.2})$$

where the complex dielectric constant ( $\epsilon = \epsilon_r + i\sigma/\omega$ ) can be rewritten as:

$$\begin{aligned} \epsilon_r(\nu) &= \text{Re}[\epsilon(\nu)] \\ \sigma(\nu) &= 2\pi\nu \text{Im}[\epsilon(\nu)] \end{aligned} \quad (\text{A.3})$$

which is the form COMSOL uses for frequency dependent dielectric media.

Constructing a material library file by hand is relatively straightforward as shown in the sample Johnson and Christy gold library below (values entered from reference [31]).

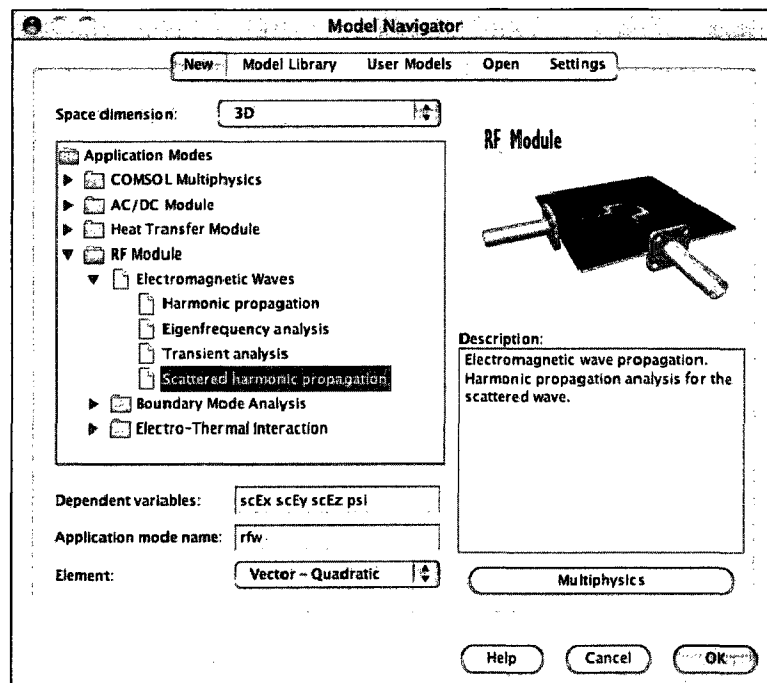
```
lib.version.name='COMSOL 3.4';
lib.name='Johnson and Christy Gold';

clear lib
lib.mat{1}.name='Gold (J&C)';
lib.mat{1}.varname='mat1';
lib.mat{1}.variables.sigma='2*pi*epsilon0_rfw*nu_rfw*jcEpsImag(nu_rfw)';
lib.mat{1}.variables.epsilonr='jcEpsReal(nu_rfw)';
clear fcns
fcns{1}.type='interp';
fcns{1}.name='jcEpsReal';
fcns{1}.method='linear';
fcns{1}.extmethod='NaN';
fcns{1}.x={'1.5475131e+14','1.8618517e+14','2.1520105e+14', ...
'2.4663491e+14','2.7565078e+14','3.0466665e+14','3.3610051e+14', ...
'3.6511638e+14','3.9655024e+14','4.2556611e+14','4.5458199e+14', ...
'4.8601585e+14','5.1503172e+14','5.4646558e+14','5.7548145e+14', ...
'6.0449732e+14','6.3593118e+14','6.6494705e+14','6.9638091e+14', ...
'7.2539679e+14','7.5441266e+14','7.8584652e+14','8.1486239e+14', ...
'8.4629625e+14','8.7531212e+14','9.0432799e+14','9.3576185e+14', ...
'9.6477772e+14','9.9621159e+14','1.0252275e+15','1.0542433e+15', ...
'1.0856772e+15','1.1146931e+15','1.1461269e+15','1.1751428e+15', ...
'1.2041587e+15','1.2355925e+15','1.2646084e+15','1.2960423e+15', ...
'1.3250581e+15','1.354074e+15','1.3855079e+15','1.4145237e+15', ...
'1.4459576e+15','1.4749735e+15','1.5039893e+15','1.5354232e+15', ...
'1.5644391e+15','1.5958729e+15'};
fcns{1}.data={'-189.042','-125.3505','-90.426461','-66.218525','-51.0496', ...
'-40.2741','-32.040669','-25.811289','-20.610164','-16.817709', ...
'-13.648209','-10.661884','-8.112669','-5.842125','-3.946161', ...
'-2.278289','-1.702701','-1.758996','-1.692204','-1.702164','-1.649404', ...
'-1.604889','-1.400625','-1.231956','-1.310241','-1.169489','-1.230804', ...
'-1.242549','-1.227421','-1.306784','-1.332261','-1.366509','-1.346409', ...
'-1.236501','-1.080444','-0.891261','-0.744529','-0.616896','-0.551009', ...
'-0.4155','-0.346329','-0.233769','-0.1325','-0.010416','0.138171', ...
'0.203899','0.292524','0.295191','0.227056'};
fcns{2}.type='interp';
fcns{2}.name='jcEpsImag';
fcns{2}.method='linear';
fcns{2}.extmethod='NaN';
fcns{2}.x = fcns{1}.x;
fcns{2}.data={'25.3552','12.5552','8.18634','5.7015','3.861','2.794', ...
'1.92542','1.62656','1.27176','1.06678','1.03516','1.37424','1.66054', ...
'2.1113','2.58044','3.81264','4.84438','5.28264','5.6492','5.71736', ...
'5.73888','5.64436','5.6092','5.598','5.53816','5.42568','5.84584', ...
'5.79258','5.78034','5.59644','5.49486','5.28242','4.97628','4.7223', ...
'4.49008','4.33846','4.16328','4.05504','3.8922','3.8252','3.7102', ...
'3.6062','3.51','3.3904','3.39682','3.32766','3.28568','3.17592', ...
'3.04128'};
lib.mat{1}.functions = fcns;
```

## Appendix B: Calculating the Near- and Far-field Properties of a Nanoshell in COMSOL

This appendix will describe how to create a basic [30, 35] nm nanoshell simulation in COMSOL Multiphysics 3.4, and compute the near- and far-field properties.

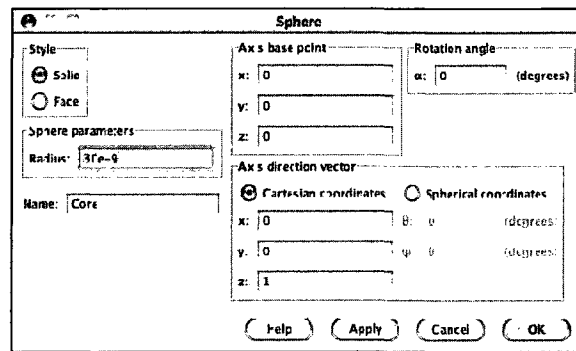
To begin the simulation, open COMSOL, chose the '3D' Space dimension, and select 'Scattered harmonic propagation' (Figure B.1).



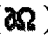
**Figure B.1.** Creating a new 3D electrodynamics simulation using the scattered field formulation.

Click the 'Sphere' icon (🔵) and enter the radius of the nanoshell core (30 nm). Repeat this step to create a gold shell with an overall radius of 35 nm, a far field transform boundary with radius 45 nm, a simulation space of radius 250 nm, and a PML layer of radius 300 nm. These parameters have been chosen to ensure the simulation

space is large enough to model the particle accurately; details on how to determine the proper simulation size for other types of particles are provided in Appendix C. The position of the far field transform boundary is arbitrary, but you may obtain more reliable results when the boundary is placed in the near field (close to the particle surface). By default, COMSOL assumes SI units.



**Figure B.2.** Creating a spherical nanoparticle core with a 30 nm radius centered at the origin.

After creating your geometry, switch to '**Boundary Mode**' () by selecting '**Boundary Settings**' under the '**Physics**' menu. Select your outer boundary in the boundaries box by clicking Index 1, and checking the '**Select by group**' box (this will select Indices 1-4, 21, 22, 31, 40). Under the '**Conditions**' tab, change the boundary type to a '**Scattering boundary condition**' with a '**Spherical wave**' originating at  $r_0 = (0, 0, 0)$  (Figure B.3).

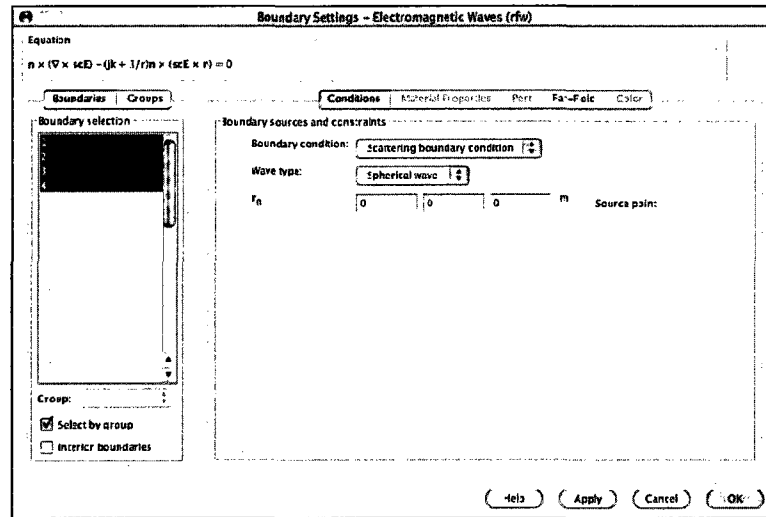


**Figure B.3.** Setting the outer boundary of the PML as a spherical scattering boundary.

Next, uncheck the **'Select by group'** box, and check **'Interior boundaries'**. Select the far field transform boundary (Indices 9-12, 25, 26, 33, 38), switch to the **'Far-field'** tab and enter **'Efar'** in the **'Name'** box (or choose your own variable name) (Figure B.4). Pressing the **'tab'** key will fill the **'Field'** and **'Normal derivative'** fields automatically. Selections of the boundaries can also be done outside of the **'Boundary selection'** list by repeatedly clicking above the desired boundary to cycle through all the boundaries and, when the desired boundary is highlighted in red, using a right click to retain that boundary in the selected group (colored blue). Selecting a boundary in your selection group (colored green) and right clicking will remove that boundary from the group.

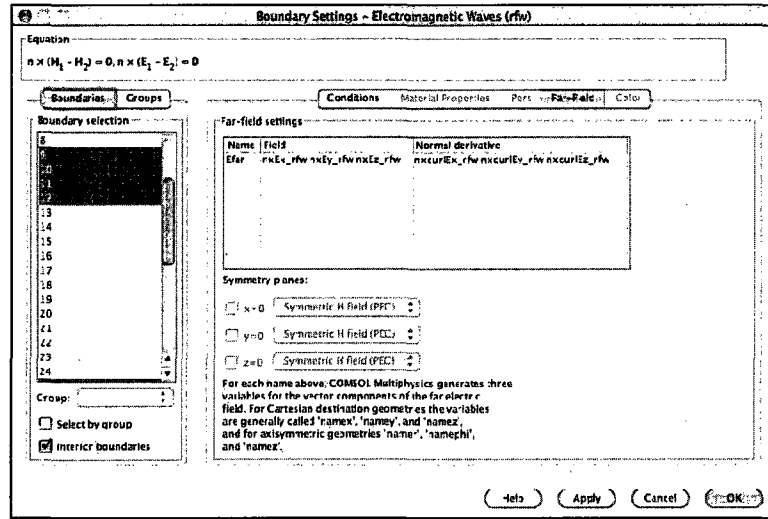


**Figure B.4.** Defining the far-field transform variable **Efar** on the far-field transform boundary.

Switch to 'Subdomain Mode' ( $\Omega$ ) by bringing up the 'Subdomain Settings' window from the 'Physics' menu, and set the outer subdomain (Index 1) to a spherical PML under the PML tab with a centerpoint of  $x_0, y_0, z_0 = (0,0,0)$  (Figure B.5).

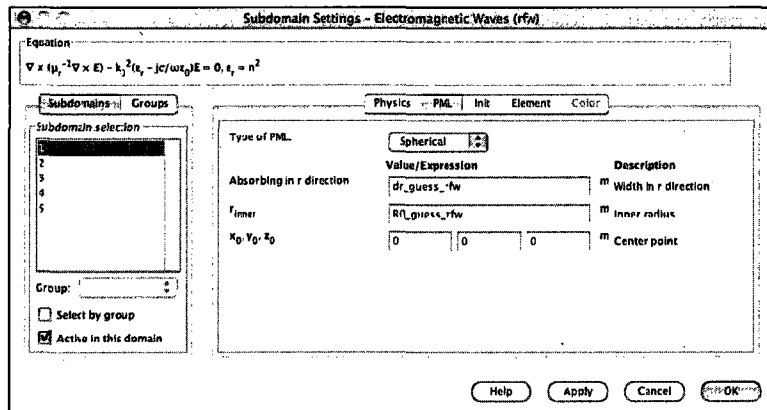
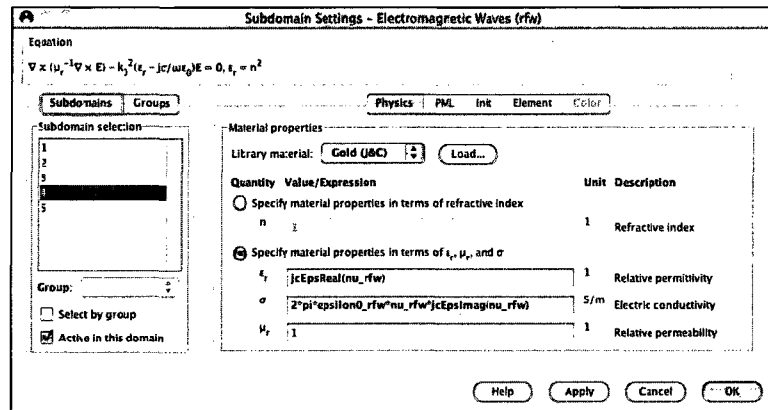


**Figure B.5.** Setting the outer subspace as an absorbing perfectly matched layer (PML) for spherical scattered waves.

For a nanoshell in vacuum, select the simulation space and PML (Indices 1-3) and check that the relative permittivity and permeability are both 1 under the 'Physics' tab. Set the core of the nanoshell (Index 5) to  $\epsilon_r = 2.04$  for silica ( $n = 1.43$ ); this is the same

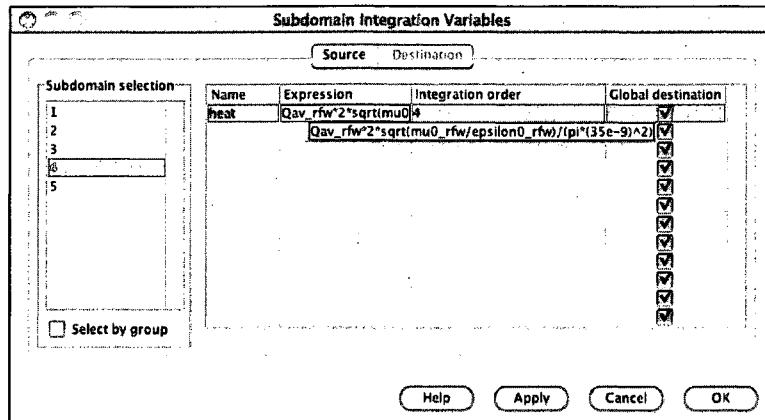


value used in gshell for Mie theory calculations of nanoshell spectra. Using the custom gold library defined and imported in Appendix A, use ‘Gold (J&C)’ as the library material for the shell subspace (Index 4) (Figure B.6).



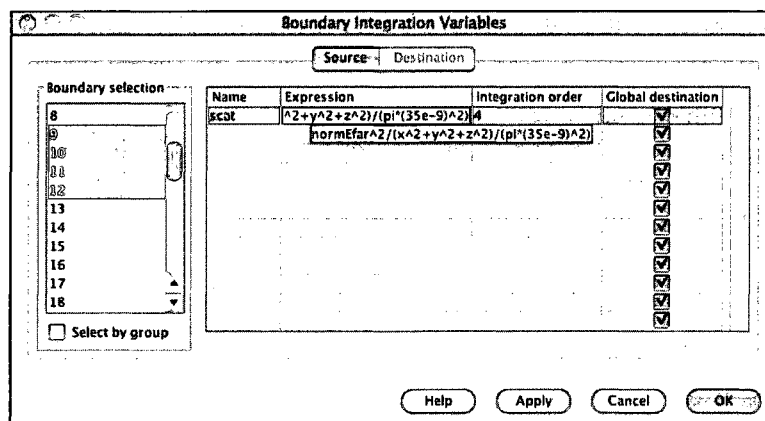
**Figure B.6.** Defining the shell subspace using the dielectric function reported by Johnson & Christy [31].

With all of the boundary conditions defined, we can now enter equations to handle the far field calculations. From the menu, select ‘Options’, ‘Integration Coupling Variables’, and then ‘Subdomain Variables.’ To calculate the far field absorption cross section, integrate the Ohmic heating in the particle divided by the particle’s cross-sectional area by defining a new variable named ‘heat’ with the expression: ‘ $Q_{av\_rfw} * 2 * \text{sqrt}(\mu_0\_rfw / \epsilonpsilon_0\_rfw) / (\pi * (35e-9)^2)$ ’ (Figure B.7).





**Figure B.7.** Calculating the far-field absorption cross section of the nanoshell.

The next step is defining the far field integral to calculate the total energy scattered into the far field. From the menu, select 'Options', 'Integration Coupling Variables', and then 'Boundary Variables.' Select the far field transform boundary (Indices 9-12, 25, 26, 33, 38), and define a new variable named 'scat' with the expression: ' $\text{normEfar}^2 / (x^2 + y^2 + z^2) / (\pi \cdot (35e-9)^2)$ ' (Figure B.8).



**Figure B.8.** Calculating the far-field scattering cross section of the nanoshell.

Create the default mesh by switching to ‘Mesh Mode’ (). Check the mesh quality using the menu option ‘Mesh’, ‘Mesh Visualization Parameters’ as shown in Figure B.9, and viewing the xy slice (). The mesh quality  $q$  is defined for a tetrahedron as:

$$q = \frac{72\sqrt{3}V}{(h_1^2 + h_2^2 + h_3^2 + h_4^2 + h_5^2 + h_6^2)^{3/2}} \quad (\text{B.1})$$

where  $V$  is the volume of the tetrahedron, and  $h_1, h_2, h_3, h_4, h_5$ , and  $h_6$  are the associated edge lengths. For a regular tetrahedron,  $q = 1$ . For all electrodynamics simulations,  $q$  should be greater than 0.1 for all mesh elements. Mesh quality can be controlled to increase simulation accuracy by adjusting the ‘Free Mesh Parameters’ to reduce the maximum mesh edge length used on the gold surface; the effects of mesh size on accuracy will be discussed further in Appendix C.

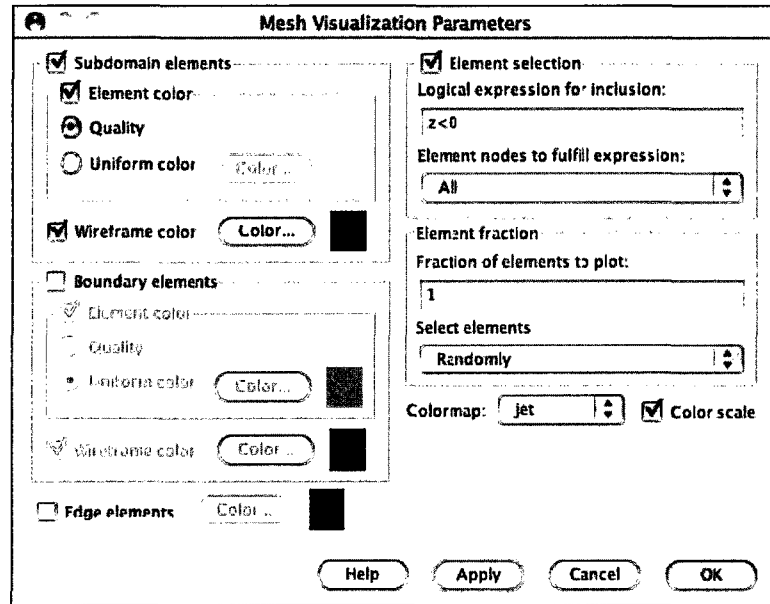


**Figure B.9.** Mesh visualization parameters for visualizing mesh quality in the  $Z = 0$  slice.

Before solving for a spectrum the simulation must be set to specify the wave using the free space wavelength under the ‘Physics’, ‘Application Mode Properties’ as shown in Figure B.10.

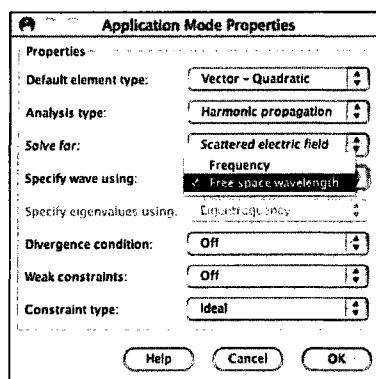


**Figure B.10.** Configure COMSOL to solve the problem in terms of the free space wavelength (frequency is the default).

Under ‘Solve’, then ‘Solver Parameters’, set the ‘Parametric’ solver to use ‘lambda0\_rfw’ as the parameter with solutions calculated at wavelengths from 550-800 nm (Figure B.11). Chose ‘Solve’, ‘Solve Problem’ (=). The problem has 78176 degrees of freedom, and takes 15 minutes (896 s) to solve on a 64 bit machine with 8G of RAM running Linux. Computing the absorption and scattering integrals takes ~30 s. All of these times will depend on the solver used, the type of processor available, whether the processor is 32- or 64-bit, and the amount of RAM installed.

Calculating the near- and far-field properties can be done using ‘Postprocessing’, ‘Global Variables Plot’ and plotting the expressions ‘heat’ and ‘scat’ as shown in Figure B.12. Near-field properties of the nanoshell can be easily visualized by selecting ‘Postprocessing’, ‘Plot Parameters...’, choosing the desired wavelength, and plotting an xy slice (Figure B.13).

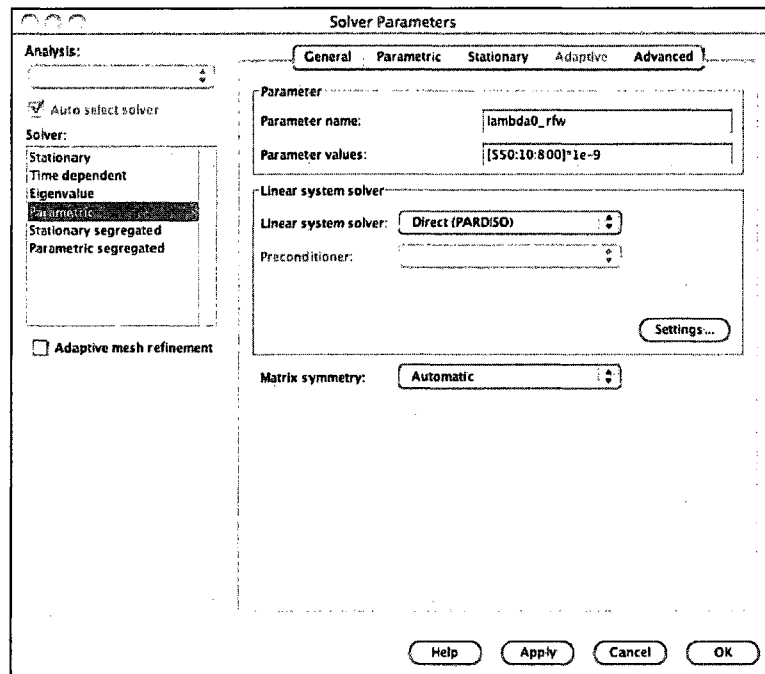


**Figure B.11.** Set the Solver Parameters to use the PARDISO linear system solver.

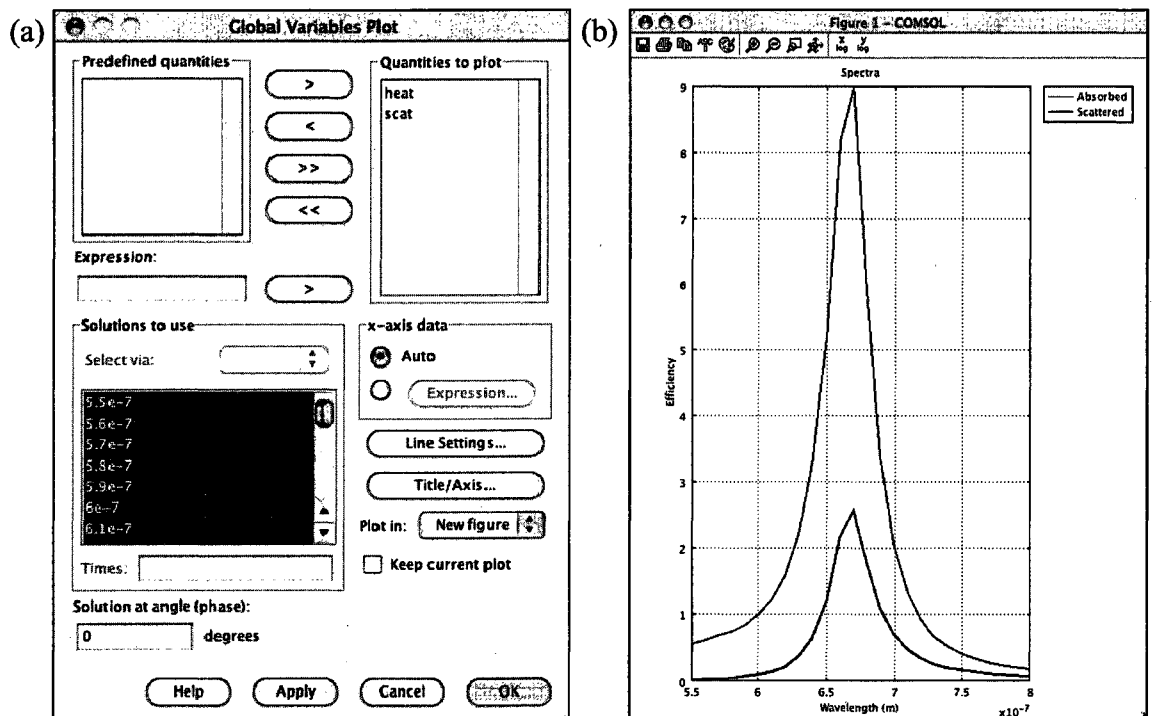


**Figure B.12.** Plotting the absorption and scattering spectra. (a) Expressions 'heat' and 'scat' plotted for all solutions, and (b) calculated spectra for the [30, 35] nm nanoshell.

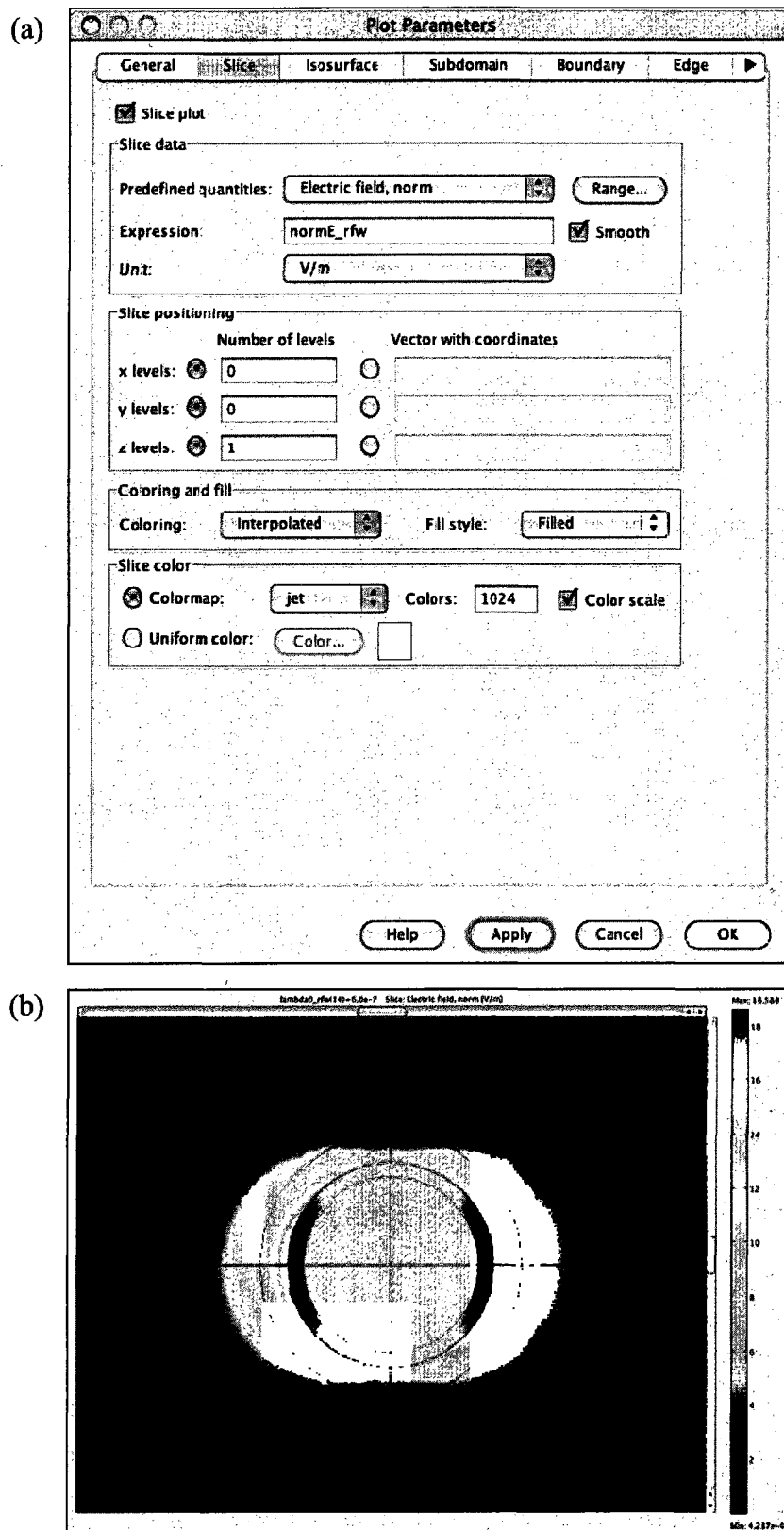


**Figure B.13.** Near-field plot (a) Plot Parameters used for making an xy slice of the near field, and (b) plot of the [30, 35] nm nanoshell near field near the dipole resonance ( $\lambda = 680$  nm).

Once a model is complete, it can be saved as an *m*-file and used as a Matlab script when using Matlab in conjunction with COMSOL. The script below will generate the results presented in this appendix:

```
% COMSOL Model of a [30, 35] nm Nanoegg
flclear fem

% Create nanoshell geometry, far field boundary, simulation space, and PMLs
g1=sphere3('30e-9','pos',{'0','0','0'},'axis',{'0','0','1'},'rot','0');
g2=sphere3('35e-9','pos',{'0','0','0'},'axis',{'0','0','1'},'rot','0');
g3=sphere3('45e-9','pos',{'0','0','0'},'axis',{'0','0','1'},'rot','0');
g4=sphere3('250e-9','pos',{'0','0','0'},'axis',{'0','0','1'},'rot','0');
g5=sphere3('300e-9','pos',{'0','0','0'},'axis',{'0','0','1'},'rot','0');

% Analyzed geometry
clear s
s.objs={g1,g2,g3,g4,g5};
s.name={'Core','Shell','FFbound','Space','PML'};
s.tags={'g1','g2','g3','g4','g5'};

fem.draw=struct('s',s);
fem.geom=geomcsg(fem);

% Initialize default mesh
fem.mesh=meshinit(fem,'hauto',5);

% Electromagnetic Waves Application Mode
clear appl
appl.mode.class = 'ElectromagneticWaves';
appl.module = 'RF';
appl.gporder = 4;
appl.cporder = 2;
appl.border = 'on';
appl.assignsuffix = '_rfw';
clear prop
prop.solvefor='ESC';
prop.inputvar='lambda';
appl.prop = prop;
clear bnd
bnd.farfield = {{{},{},{'Efar';'nxEx_rfw nxEy_rfw nxEz_rfw';'nxcurlEx_rfw
nxcurlEy_rfw nxcurlEz_rfw';'ref'}}};
bnd.wavetype = {'sphere','plane','plane'};
bnd.type = {'SC','cont','cont'};
bnd.ind = [1,1,1,1,2,2,2,2,3,3,3,3,2,2,2,2,2,2,2,1,1,2,2,3,3,2,2,2,2, ...
1,2,3,2,2,2,2,3,2,1];
appl.bnd = bnd;
clear equ
equ.epsilonr = {1,1,'mat1_jcEpsReal(nu_rfw)',2.04};
equ.stype = {'sph','none','none','none'};
equ.sigma = {0,0,'2*pi*epsilon0_rfw*nu_rfw*mat1_jcEpsImag(nu_rfw)',0};
equ.ind = [1,2,2,3,4];
appl.equ = equ;
fem.appl{1} = appl;
fem.frame = {'ref'};
fem.border = 1;
clear units;
```

```

units.basesystem = 'SI';
fem.units = units;

% Integration coupling variables for calculating far-field spectra
clear elemcpl
clear elem
elem.elem = 'elcplscalar';
elem.g = {'1'};
src = cell(1,1);
clear bnd
bnd.expr = {{{{},{},{'normEfar^2/(x^2+y^2+z^2)/(pi*(35e-9)^2)'},{}}};
bnd.ipoints = {{{{},{},{'4'}}}};
bnd.frame = {{{{},{},{'ref'}}}};
bnd.ind = {{{{'1','2','3','4','5','6','7','8','13','14','15','16','17', ...
'18','19','20','21','22','23','24','27','28','29','30','31','32','34', ...
'35','36','37','39','40'}},{'9','10','11','12','25','26','33','38'}}}};
clear equ
equ.expr = {{{{},{},{'Qav_rfw*2*sqrt(mu0_rfw/epsilon0_rfw)/(pi*(35e-9)^2)'}}}};
equ.ipoints = {{{{},{},{'4'}}}};
equ.frame = {{{{},{},{'ref'}}}};
equ.ind = {{{{'1','2','3','5'}}},{'4'}};
src{1} = {{{{},{},bnd,equ}}};
elem.src = src;
geomdim = cell(1,1);
geomdim{1} = {};
elem.geomdim = geomdim;
elem.var = {'scat','heat'};
elem.global = {'1','2'};
elemcpl{1} = elem;
fem.elemcpl = elemcpl;

% Johnson and Christy Gold Library
clear lib
lib.mat{1}.name='Gold (J&C)';
lib.mat{1}.varname='mat1';
lib.mat{1}.variables.sigma='2*pi*epsilon0_rfw*nu_rfw*jcEpsImag(nu_rfw)';
lib.mat{1}.variables.epsilonr='jcEpsReal(nu_rfw)';
clear fcns
fcns{1}.type='interp';
fcns{1}.name='jcEpsReal';
fcns{1}.method='linear';
fcns{1}.extmethod='NaN';
fcns{1}.x={'1.5475131e+14','1.8618517e+14','2.1520105e+14', ...
'2.4663491e+14','2.7565078e+14','3.0466665e+14','3.3610051e+14', ...
'3.6511638e+14','3.9655024e+14','4.2556611e+14','4.5458199e+14', ...
'4.8601585e+14','5.1503172e+14','5.4646558e+14','5.7548145e+14', ...
'6.0449732e+14','6.3593118e+14','6.6494705e+14','6.9638091e+14', ...
'7.2539679e+14','7.5441266e+14','7.8584652e+14','8.1486239e+14', ...
'8.4629625e+14','8.7531212e+14','9.0432799e+14','9.3576185e+14', ...
'9.6477772e+14','9.9621159e+14','1.0252275e+15','1.0542433e+15', ...
'1.0856772e+15','1.1146931e+15','1.1461269e+15','1.1751428e+15', ...
'1.2041587e+15','1.2355925e+15','1.2646084e+15','1.2960423e+15', ...
'1.3250581e+15','1.354074e+15','1.3855079e+15','1.4145237e+15', ...
'1.4459576e+15','1.4749735e+15','1.5039893e+15','1.5354232e+15', ...
'1.5644391e+15','1.5958729e+15'};
fcns{1}.data={'-189.042','-125.3505','-90.426461','-66.218525','-51.0496', ...
'-40.2741','-32.040669','-25.811289','-20.610164','-16.817709', ...
'-13.648209','-10.661884','-8.112669','-5.842125','-3.946161', ...
'-2.278289','-1.702701','-1.758996','-1.692204','-1.702164','-1.649404', ...
'-1.604889','-1.400625','-1.231956','-1.310241','-1.169489','-1.230804', ...
'-1.242549','-1.227421','-1.306784','-1.332261','-1.366509','-1.346409', ...
'-1.236501','-1.080444','-0.891261','-0.744529','-0.616896','-0.551009', ...
'-0.4155','-0.346329','-0.233769','-0.1325','-0.010416','0.138171', ...

```



```

'0.203899','0.292524','0.295191','0.227056'};
fcns{2}.type='interp';
fcns{2}.name='jcEpsImag';
fcns{2}.method='linear';
fcns{2}.extmethod='NaN';
fcns{2}.x = fcns{1}.x;
fcns{2}.data={'25.3552','12.5552','8.18634',' 5.7015',' 3.861',' 2.794', ...
'1.92542','1.62656','1.27176','1.06678','1.03516','1.37424','1.66054', ...
' 2.1113','2.58044','3.81264','4.84438','5.28264',' 5.6492','5.71736', ...
'5.73888','5.64436',' 5.6092',' 5.598','5.53816','5.42568','5.84584', ...
'5.79258','5.78034','5.59644','5.49486','5.28242','4.97628',' 4.7223', ...
'4.49008','4.33846','4.16328','4.05504',' 3.8922',' 3.8252',' 3.7102', ...
' 3.6062',' 3.51',' 3.3904','3.39682','3.32766','3.28568','3.17592', ...
'3.04128'};
lib.mat{1}.functions = fcns;

fem.lib = lib;

% ODE Settings
clear ode
clear units;
units.basesystem = 'SI';
ode.units = units;
fem.ode=ode;
% Multiphysics
fem=multiphysics(fem);

% Generate GMC mesh cases
fem=meshcaseadd(fem,'mgauto','shape');

% Extend mesh
fem.xmesh=mesnextend(fem);
fem.sol=femstatic(fem, ...
'solcomp',{'tscExscEyscEz10','tscExscEyscEz20','tscExscEyscEz21'}, ...
'outcomp',{'tscExscEyscEz10','tscExscEyscEz20','tscExscEyscEz21'}, ...
'pname','lambda0_rfw', ...
'plist',[[550:10:800]*1e-9], ...
'oldcomp',{}, ...
'linsolver','pardiso');

```

## Appendix C: Space and Meshing Effects

The size of the simulation space and the mesh density at the surface of the nanoparticle can strongly affect the calculated near and far field properties if not chosen correctly. Careful convergence testing, however, can allow the determination of the correct plasmonic properties of an arbitrary structure. This appendix presents a method for determining the minimum simulation space volume and maximum surface mesh density required to accurately model a nanoparticle (Figure C.1). Optimizing these two parameters reduces the number of degrees of freedom which, in turn, reduces the computational cost of calculating a spectrum.

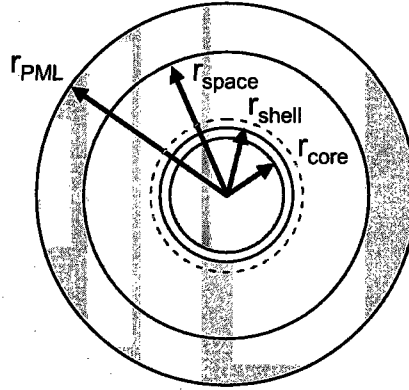


**Figure C.1.** Schematic of the simulation space. While testing for convergence the PML thickness ( $r_{\text{PML}} - r_{\text{space}} = 50$  nm), the nanoshell size ( $[r_{\text{core}}, r_{\text{shell}}] = [30, 35]$  nm), and the far field transform boundary position (dotted grey line) all remain constant.

Using the  $[30, 35]$  nm nanoshell modeled in Appendix B, and decreasing the simulation space radius from  $r_{\text{space}} = 200$  nm, where the simulation converges to the far field Mie theory extinction spectrum, to  $r_{\text{space}} = 50$  nm will cause the dipole peak to weaken, broaden, and redshift (Figure C.2). Using the dipole extinction efficiency

determined using Mie theory, the maximum extinction cross section is  $C_{ext} \cdot \pi \cdot (r_{space})^2$ , where  $C_{ext}$  is the extinction cross section at the dipole peak. Since the particle cannot absorb or scatter more energy than is injected into the system by the incident plane wave, the spectrum must be incorrect for all  $A_{space}/C_{ext} < 1$ ; determining the exact size of the space required can be done iteratively. For particles without an analytical solution, iteratively determining the minimum required simulation space size must be done to avoid computational artifacts in the spectrum.

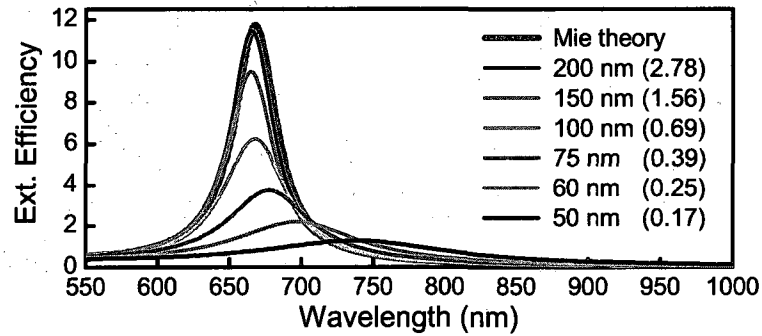


**Figure C.2.** Extinction spectra calculated with the simulation space radius changing relative to the nanoshell radius, where each spectra is labeled according to the radius of the simulation space, and the ratio  $A_{space}/C_{ext}$ . The analytical and FEM solutions agree for  $r_{space} > 200$  nm ( $A_{space}/C_{ext} > 3$ ).

Determining if the simulation space is sufficiently large can be done by increasing the simulation space until all the desired parameters (dipole peak wavelength, peak width, extinction efficiency, and near-field enhancement) converge to constant values (Figure C.3). The last parameter to converge to a constant value will be the near-field enhancement, which is also the least computationally intensive parameter to measure, as no integration is required. However, as shown in Figure C.3(d), the near-field

enhancements calculated using the default mesh may not be correct even if all the far-field properties have converged to the correct value.

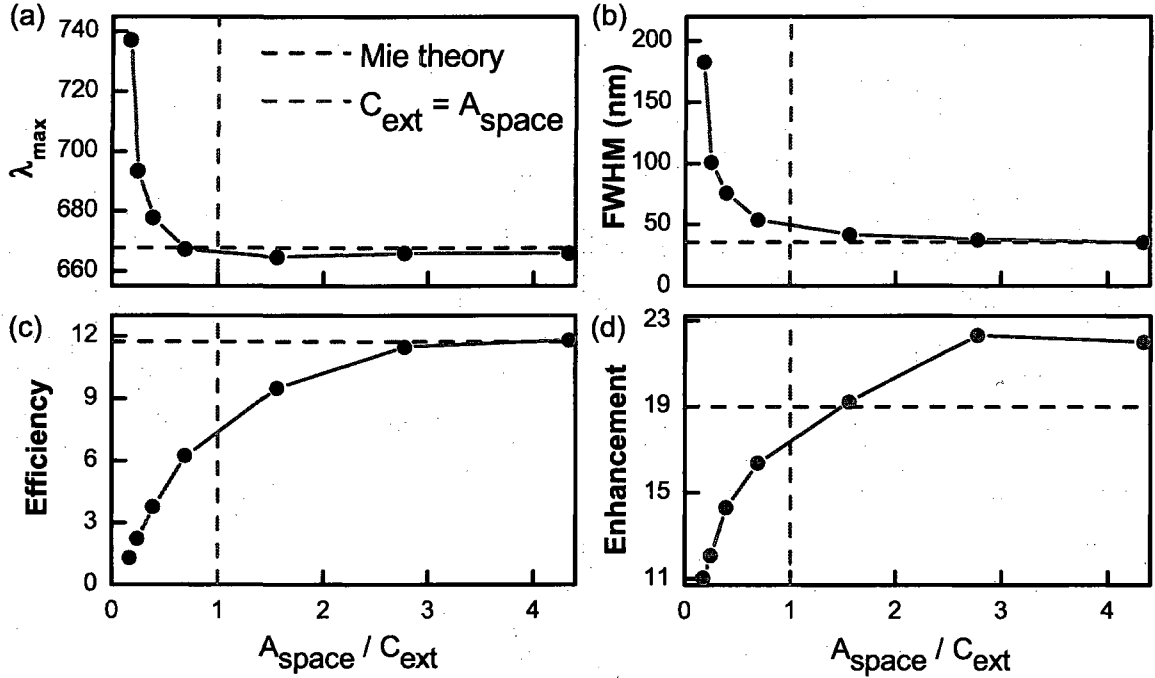


**Figure C.3.** Convergence tests at the dipole peak for (a) peak wavelength, (b) FWHM of the peak, (c) peak amplitude, and (d) maximum near-field enhancement. Simulation spaces with a cross sectional area less than 3x the extinction cross section of the nanoparticle do not converge to the analytical solution.

Obtaining the correct near-field properties can be done by increasing the mesh density on the surface of the plasmonic particle, where the field gradients will be largest, while holding the simulation space at a constant size where the far-field properties have converged. As the mesh density decreases, the maximum near-field enhancements will jump randomly then, given a sufficiently dense mesh, converge to the analytical solution (Figure C.4).

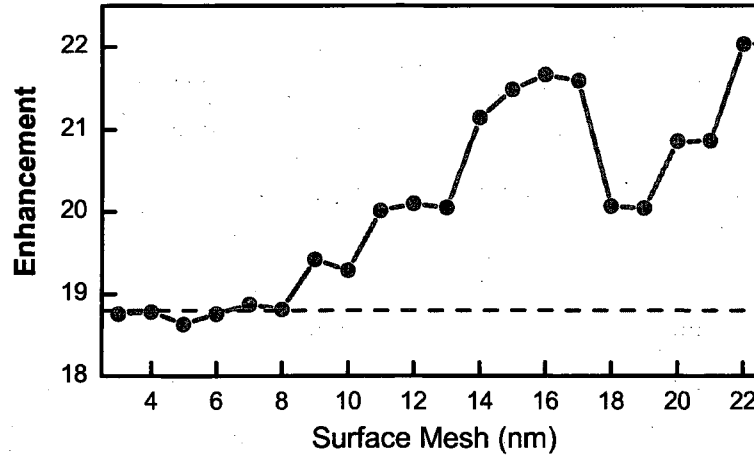


**Figure C.4.** Dependence of the near-field enhancement on mesh size at the particle surface.

This method provides a general scheme for determining the convergence of an arbitrary particle's near- and far-field properties in COMSOL:

1. Increase the simulation space size until the far-field properties converge to a constant value.
2. Using a simulation space with converged far-field properties, decrease the mesh density on the surface of the nanoparticle until the near-field converges to a constant value.

The first step requires computing a course spectrum to determine the unknown peak wavelength. Once the wavelength corresponding to maximum extinction ( $\lambda_{\max}$ ) is known the second step only requires computing values at  $\lambda_{\max}$ . This process must be repeated for each incident E-field polarization, as the extinction cross section may change.